

Searching for Heavy Leptophilic Z' : from Lepton Colliders to Gravitational Waves

Arnab Dasgupta,^{1,*} P. S. Bhupal Dev,^{2,†} Tao Han,^{1,‡}
Rojalin Padhan,^{1,3,4,§} Si Wang,^{1,¶} and Keping Xie^{1,5,**}

¹*Pittsburgh Particle Physics, Astrophysics, and Cosmology Center,
Department of Physics and Astronomy, University of Pittsburgh, Pittsburgh, PA 15206, USA*

²*Department of Physics and McDonnell Center for the Space Sciences,
Washington University, St. Louis, MO 63130, USA*

³*Institute of Physics, Sachivalaya Marg, Bhubaneswar 751005, Odisha, India*

⁴*Homi Bhabha National Institute, BARC Training School Complex, Anushakti Nagar, Mumbai 400094, India*

⁵*Department of Physics and Astronomy, Michigan State University, East Lansing, MI 48824, USA*

We study the phenomenology of leptophilic Z' gauge bosons at the future high-energy e^+e^- and $\mu^+\mu^-$ colliders, as well as at the gravitational wave observatories. The leptophilic Z' model, although well-motivated, remains largely unconstrained from current low-energy and collider searches for Z' masses above $\mathcal{O}(100 \text{ GeV})$, thus providing a unique opportunity for future lepton colliders. Taking $U(1)_{L_\alpha-L_\beta}$ ($\alpha, \beta = e, \mu, \tau$) models as concrete examples, we show that future e^+e^- and $\mu^+\mu^-$ colliders with multi-TeV center-of-mass energies provide unprecedented sensitivity to heavy leptophilic Z' bosons. Moreover, if these $U(1)$ models are classically scale-invariant, the phase transition at the $U(1)$ symmetry-breaking scale tends to be strongly first-order with ultra-supercooling, and leads to observable stochastic gravitational wave signatures. We find that the future sensitivity of gravitational wave observatories, such as advanced LIGO-VIRGO and Cosmic Explorer, can be complementary to the collider experiments, probing higher Z' masses up to $\mathcal{O}(10^4 \text{ TeV})$, while being consistent with naturalness and perturbativity considerations.

CONTENTS

I. Introduction	2
II. Leptophilic Z' and current constraints	3
A. $U(1)_{L_\alpha-L_\beta}$ models	3
B. Current laboratory bounds on the model parameters	5
III. Z' phenomenology at future lepton colliders	7
A. The Z' resonance production	8
B. Off-shell Z' production	13
C. $Z' + \gamma$ associated production	14
D. Mono-photon final state	16
E. Four-lepton final states	16
F. Sensitivity summary	18
IV. Gravitational wave signal	20
A. Effective potential and thermal corrections	21
B. Strong first-order phase transition	23

* arnabdasgupta@pitt.edu

† bdev@wustl.edu

‡ than@pitt.edu

§ rojalin.p@iopb.res.in

¶ siw34@pitt.edu

** xiekening@pitt.edu

C. Gravitational wave spectrum	26
D. Complementarity with other laboratory constraints	29
E. Theoretical constraints	30
V. Summary and Conclusions	31
Acknowledgments	32
References	32

I. INTRODUCTION

High-energy colliders have immensely enriched our understanding of nature at the most fundamental level. The Large Hadron Collider (LHC), in particular, has enabled the exploration of energy scales as high as several TeV, and has consolidated the robustness of the Standard Model (SM). However, the primary pursuit of the LHC, namely, finding beyond-the-SM (BSM) phenomena, remains elusive. Despite tremendous efforts of theoretical and experimental works to address the empirical and theoretical shortcomings of the SM, no sign of BSM physics has been observed so far, and stringent bounds (up to several TeV) have been placed on their mass scale [1]. Given all these constraints, one might wonder whether the scale of BSM physics must lie *beyond* the energy scales accessible at the LHC.

There is one notable loophole in this general argument for hadron colliders, *viz.*, if the new resonance is electrically neutral and couples only to the SM leptons at leading order. Most of the LHC (and Tevatron) bounds coming from resonance searches do not directly apply to such a neutral *leptophilic* sector. The relevant collider constraints in this case mainly come from LEP (or from LHC via higher-order processes), and are generally much weaker than the direct LHC constraints applicable for hadrophilic resonances. The LEP constraints from resonance searches are typically around the 100 GeV scale, limited by its center-of-mass energy of $\sqrt{s} = 209$ GeV, whereas the LEP contact interaction bounds for heavier particles are at most in the TeV range (for $\mathcal{O}(1)$ couplings) [2, 3]. Therefore, future lepton colliders, such as the proposed e^+e^- colliders like ILC [4], CEPC [5], FCC-ee [6], and CLIC [7], or a high-energy $\mu^+\mu^-$ collider [8–11], are uniquely capable of probing leptophilic BSM particles to unprecedented mass and coupling values. In this paper, we will focus on leptophilic neutral gauge bosons (Z') as a case study to illustrate this point.

At first sight, new neutral gauge bosons, especially coupling only to leptons and not to quarks at tree level, may look artificial. However, there are good symmetry reasons that can motivate such a scenario. First of all, the presence of additional Abelian symmetries like $U(1)$ is quite natural and can be motivated by Grand Unified Theories, string compactifications, extra dimensional models, solutions of the gauge hierarchy problem, and so on [12], which always come with the corresponding Z' bosons after the $U(1)$ -symmetry breaking. As for the leptophilic nature of Z' , it is well-known that the classical SM Lagrangian already contains the accidental global symmetry $U(1)_e \times U(1)_\mu \times U(1)_\tau$, associated with conserved lepton number for each family. A simple $U(1)$ gauge extension of the SM allows us to promote $U(1)_{L_\alpha - L_\beta}$ (where $\alpha, \beta = e, \mu, \tau$ with $\alpha \neq \beta$) to an anomaly-free local gauge symmetry [13–15]. The associated Z' gauge bosons are *naturally* leptophilic, with couplings to quarks induced only at the loop level. Therefore, the most stringent dijet constraints on heavy Z' coming from Tevatron and LHC [16] are not applicable in this scenario, thus opening up a large swath of parameter space in the Z' mass-coupling plane.¹ In this paper, we target this currently unexplored leptophilic Z' parameter space and study the future lepton collider prospects of probing this well-motivated BSM scenario. We consider all possible production channels (both resonance and off-resonance, associated production with photons, and final-state radiation) to carve out the future lepton collider sensitivity in the Z' parameter space. Taking $\sqrt{s} = 3$ TeV electron/muon collider with an integrated luminosity of 1 ab^{-1} as a case study, we find up to three orders of magnitude

¹ Such a leptophilic Z' can also serve as a portal to the dark sector, with very interesting phenomenology [17–22].

improvement over the existing constraints for the Z' coupling sensitivity reach over a broad mass range.

Another interesting and complementary aspect of the leptophilic $U(1)$ models we study here is the cosmological phase transition of the $U(1)$ -symmetry-breaking scalar field. If the symmetry is classically conformal [23], the tree-level potential is flat due to scale-invariance, and thermal corrections can easily dominate and make the phase transition strongly first order [24], leading to a potentially observable stochastic gravitational wave (GW) signal. The conformal invariance is motivated as a possible solution to the gauge hierarchy problem in the SM. It is well-known that the fermion masses in the SM are protected by chiral symmetry, i.e. in the limit of $m_f \rightarrow 0$, radiative corrections δm_f also vanish to all orders in perturbation theory [25]. However, this is not the case for the Higgs boson mass, where the radiative correction δm_h does not vanish in the limit of $m_h \rightarrow 0$. It leads to the puzzle of the stabilization of the weak scale against large radiative corrections – the so-called gauge hierarchy problem [26, 27]. This can, in principle, be evaded in a classical conformal theory [28], where all the mass scales (including the electroweak scale) are generated by dimensional transmutation using the Coleman-Weinberg mechanism [29]. However, this mechanism cannot be applied directly to the SM Higgs sector since the predicted Higgs mass is too low, and moreover, the Coleman-Weinberg effective potential in the SM becomes unbounded from below [30]. Instead, the $U(1)$ models provide a viable alternative to realize the conformal invariance [31–36]. We study the interconnection and the complementarity of our collider signals with the GW signal in classically conformal versions of the leptophilic $U(1)_{L_\alpha-L_\beta}$ models. We show that the current GW data from aLIGO-aVIRGO [37] already excludes a portion of the $U(1)_{L_\alpha-L_\beta}$ model parameter space at high $M_{Z'}$ values not accessible to colliders, whereas the next-generation GW experiments in the mHz-kHz regime, such as μ ARES [38], LISA [39], DECIGO [40], BBO [41], ET [42], and CE [43] will further extend the sensitivity reach to our Z' parameter space of interest. We also comment on the possibility of explaining the recent Pulsar Timing Array observations of stochastic GW at nHz frequencies [44–47] in these models.

The rest of the paper is organized as follows. In Section II, we briefly discuss the leptophilic Z' models under consideration and summarize the existing bounds on the model parameter space. In Section III, we analyze various production channels for the Z' boson at future lepton colliders, and summarize the sensitivity limits. In Section IV, we study the GW signals in a conformal version of the $U(1)$ models. Our conclusions are given in Section V.

II. LEPTOPHILIC Z' AND CURRENT CONSTRAINTS

A. $U(1)_{L_\alpha-L_\beta}$ models

Within the particle content of the SM, it is possible to gauge one of the three combinations of $L_\alpha - L_\beta$ ($\alpha, \beta = e, \mu, \tau$), without introducing an anomaly [13–15]. This surprising feature is the main motivation behind the minimal BSM framework considered here, with the SM gauge symmetry extended by an extra leptophilic $U(1)_{L_\alpha-L_\beta}$, such that only two lepton flavors α and β are oppositely charged, while all other SM fields are neutral under this $U(1)$ gauge symmetry. It is interesting to note that although we can formally consider the anomaly-free combination $U(1)_{L_e-L_\mu} \times U(1)_{L_\mu-L_\tau} \times U(1)_{L_e-L_\tau}$, the decomposition $L_e-L_\tau = (L_e-L_\mu) + (L_\mu-L_\tau)$ shows that not all of their generators are independent and only two of the lepton number differences can be gauged. The question then arises of which subgroup should be chosen. The $L_\mu - L_\tau$ option is the most popular of the three, because (a) it predicts the neutrino mass matrix to be $L_\mu - L_\tau$ symmetric, which (with a small symmetry-breaking effect) fits the observed neutrino oscillation data very well [48–52], and (b) it provides a simple solution to the muon $g - 2$ anomaly [53–55]. See Refs. [56–74] for various phenomenological studies of the $U(1)_{L_\mu-L_\tau}$ model. The other two combinations $U(1)_{L_e-L_\mu}$ and $U(1)_{L_e-L_\tau}$ have also been considered in various contexts [75–80]. Here we will be agnostic of the possible flavor-gauge connection, and will primarily focus on the future lepton collider phenomenology of each of the three combinations of $U(1)_{L_\alpha-L_\beta}$ separately.

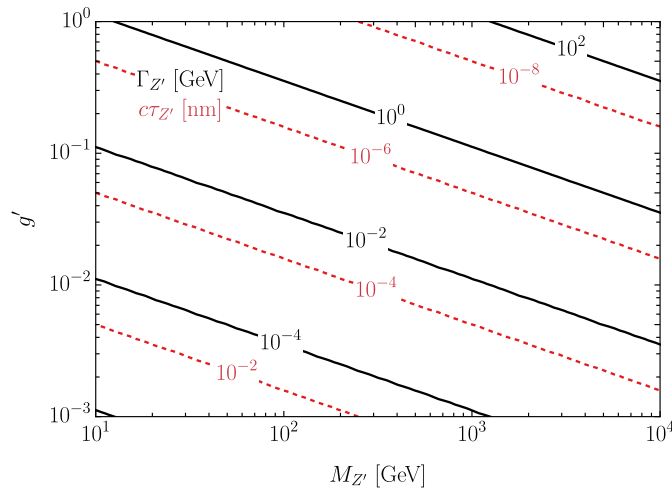


FIG. 1. Dependence of Z' decay width $\Gamma_{Z'}$ (solid contours) and the corresponding proper decay length $c\tau_{Z'}$ (dashed contours) on its mass $M_{Z'}$ and gauge coupling g' in the $U(1)_{L_\alpha-L_\beta}$ model.

The $U(1)_{L_\alpha-L_\beta}$ gauge involves only two lepton flavors, with the allowed Z' decay channels as²

$$Z' \rightarrow \ell_\alpha^+ \ell_\alpha^-, \ell_\beta^+ \ell_\beta^-, \nu_\alpha \bar{\nu}_\alpha, \nu_\beta \bar{\nu}_\beta. \quad (5)$$

Considering $M_{Z'} \gg m_\ell$, we can safely ignore the lepton mass in Eq. (4), and obtain the total width of Z' as

$$\Gamma_{Z'} \simeq \frac{(2N_\ell + N_\nu)g'^2}{24\pi} M_{Z'} = \frac{g'^2}{4\pi} M_{Z'}, \quad (6)$$

where $N_\ell = N_\nu = 2$ for two lepton flavors. Note that each neutrino flavor only contributes half to Eq. (4) because of its left-handed chirality. Here we do not consider the potential Z' interactions with right-handed neutrinos or with dark sector.

In Fig. 1, we present the Z' decay width with respect to its mass $M_{Z'}$ and the corresponding gauge coupling g' . We see that for the parameter region of our current interest, *i.e.*, $M_{Z'} \in [10, 10^4]$ GeV with $g' \in [10^{-3}, 1]$, the Z' decay width spans the range $\sim [10^{-6}, 10^2]$ GeV. The proper decay length can be estimated by

$$c\tau_{Z'} = \frac{c}{\Gamma_{Z'}} = 2.5 \times 10^{-4} \text{ nm} \left(\frac{10^{-2}}{g'} \right)^2 \left(\frac{100 \text{ GeV}}{M_{Z'}} \right), \quad (7)$$

shown as red dashed lines in Fig. 1. We see that Z' will decay promptly in the parameter space of our interest, which can potentially leave direct or indirect signals at colliders. Based on this knowledge, we will focus on the Z' production followed by its prompt decay in the rest of this work.

B. Current laboratory bounds on the model parameters

In this section, we summarize the existing constraints on the $U(1)_{L_\alpha-L_\beta}$ gauge boson mass $M_{Z'}$ and coupling g' , as shown in Fig. 2 and explained below. This is the most comprehensive set of constraints on these models available to date for our region of interest, *i.e.*, for $M_{Z'} > 10$ GeV; for other constraints relevant in the low-mass regime, see *e.g.*, the summary plots in Refs. [86, 87]. All the constraints shown here are at 95% confidence level (CL), unless otherwise specified.

- $(g - 2)_\ell$: The new interaction between Z' and the SM leptons will give a contribution to the

² The coupling of Z' to the third lepton flavor is induced at loop level via $\gamma - Z'$ mixing, which is however suppressed by $m_{\ell_{\alpha,\beta}}^2/M_{Z'}^2$ [85].

anomalous magnetic dipole moment $a_\ell = (g - 2)_\ell/2$ of the corresponding leptons as [88, 89]

$$\Delta a_\ell \simeq \frac{g'^2}{4\pi^2} \int_0^1 dx \frac{m_\ell^2 x^2 (1-x)}{m_\ell^2 x^2 + M_{Z'}^2 (1-x)} \simeq \frac{g'^2 m_\ell^2}{12\pi^2 M_{Z'}^2} \quad (8)$$

for $M_{Z'} \gg m_\ell$. For a_e , although the experimental value is known very precisely [90], the SM prediction [91] relies on the measurement of the fine-structure constant using the recoil velocity/frequency of atoms that absorb a photon, and currently there is a 5.5σ discrepancy between the measurements using Rubidium-87 [92] and Cesium-133 [93]. When translated into Δa_e , they give

$$\Delta a_e = \begin{cases} (4.8 \pm 3.0) \times 10^{-13} & (\text{Rb}) \\ (-8.8 \pm 3.6) \times 10^{-13} & (\text{Cs}) \end{cases} . \quad (9)$$

Since the correction from Z' loop is of positive sign (cf. Eq. (8)), we use the Rb-measurement and show the 95% CL upper limit in Fig. 2 (labeled as $(g - 2)_e$), which goes like $g' \lesssim 2.2 \times 10^{-2} M_{Z'}/\text{GeV}$, and is applicable to the $U(1)_{L_e-L_\alpha}$ models.

As for a_μ , the Muon $g-2$ Collaboration combined the recent Fermilab measurements [94, 95] with the old Brookhaven E821 result [96], and obtained a 5.0σ deviation from the world average of the SM expectation [97]:

$$\Delta a_\mu = (2.49 \pm 0.48) \times 10^{-9} . \quad (10)$$

This discrepancy is reduced to only about 2σ , if the ab initio lattice simulation result from BMW Collaboration [98] is used for the SM result. However, this claim is being independently verified by other lattice groups [99–103], and until the issue is settled, we prefer to use Eq. (10) to derive the 95% CL-preferred region in the Z' parameter space, as shown by the orange-shaded band in Fig. 2. Moreover, it gives a 5σ exclusion bound of $g' \lesssim 7.6 \times 10^{-3} M_{Z'}/\text{GeV}$, applicable to both $U(1)_{L_e-L_\mu}$ and $U(1)_{L_\mu-L_\tau}$ models.

In comparison, a_τ is known relatively poorly. The current experimental limits are

$$a_\tau = \begin{cases} [-0.052, 0.013] & (\text{DELPHI 95\% CL [104]}) \\ [-0.057, 0.024] & (\text{ATLAS 95\% CL [105]}) \\ 0.001_{-0.089}^{+0.055} & (\text{CMS 68\% CL [106]}) \end{cases} . \quad (11)$$

A global analysis of LEP and SLD data on the τ -lepton pair production in an effective field theory framework yields a slightly tighter constraint: $a_\tau = [-0.007, 0.005]$ at 95% CL level [107]. An even better bound of $|a_\tau| < 1.8 \times 10^{-3}$ at 95% CL was obtained recently using the full LHC Run 2 data on tau-pair production [108]. Taking the leading one-loop QED result for the SM prediction, $a_\tau^{\text{SM}} = \alpha/2\pi \simeq 1.16 \times 10^{-3}$ [109], we get a 95% CL bound on $|\Delta a_\tau| < 6.4 \times 10^{-4}$, which translates into a rather weak bound of $g' \lesssim 0.15 M_{Z'}/\text{GeV}$, applicable to $U(1)_{L_\alpha-L_\tau}$ models. This, however, falls outside the range shown in Fig. 2.

- **Neutrino trident production:** Another strong bound comes from the production of a muon-antimuon pair in the scattering of muon neutrinos in the Coulomb field of a target nucleus, *e.g.*, neutrino trident production [110]. A combination of measurements of the trident cross-section from CHARM-II [111], CCFR [112] and NuTeV [113] imposes a bound of $g' \lesssim 1.9 \times 10^{-3} M_{Z'}/\text{GeV}$ on the $U(1)_{L_e-L_\mu}$ and $U(1)_{L_\mu-L_\tau}$ models [114], as shown in Fig. 2 by the purple shaded region. This trident bound rules out the region preferred by the $(g - 2)_\mu$ anomaly in the entire high mass range.³
- **Neutrino scattering:** The interaction between Z' and electrons contributes to the elastic $\bar{\nu}_e + e^- \rightarrow \bar{\nu}_e + e^-$ scattering process in $U(1)_{L_e-L_\alpha}$ models [20, 79]. Using the $\nu_e - e$ elastic scattering cross-section measurement from LSND [116], we obtain a 95% CL bound of $g' \lesssim 3 \times 10^{-3} M_{Z'}/\text{GeV}$ [20], as shown in Fig. 2 by blue shaded area. Similarly, the $\bar{\nu}_e e^-$ scattering cross-

³ There still exists some allowed parameter space in the $U(1)_{L_\mu-L_\tau}$ model that can explain the $(g - 2)_\mu$ anomaly for a lighter $M_{Z'} \sim 10\text{--}100$ MeV and $g' \sim 10^{-3}$ [65]. This region can be probed in low-energy experiments like NA64-e [115].

section has been measured by TEXONO [117], which sets a limit of $g' \lesssim 1.7 \times 10^{-3} M_{Z'}/\text{GeV}$ [79, 87, 118]. This constraint is shown by the green shaded region in Fig. 2.

- **IceCube:** The Z' couplings with SM neutrinos and electrons will introduce non-standard neutrino interactions (NSI), which impact the neutrino-matter effective potential [119, 120]. The NSI can be parametrized as $\varepsilon_{\alpha\beta} = g'^2/\sqrt{2}G_F M_{Z'}^2$, where $G_F \simeq 1.166 \times 10^{-5} \text{ GeV}^{-2}$ is the Fermi constant. Using the 8-year IceCube DeepCore data, a preliminary 90% CL bound on $|\varepsilon_{\tau\tau} - \varepsilon_{\mu\mu}| \leq 2.1 \times 10^{-2}$ has been obtained [121], which is stronger by a factor of few from the published limits from IceCube [122] and ANTARES [123], and by almost an order of magnitude stronger than the Super-Kamiokande limit [124]. The NSI constraint translates into a bound of $g' \lesssim 5.9 \times 10^{-4} M_{Z'}/\text{GeV}$, which applies to the $U(1)_{L_e-L_\mu}$ and $U(1)_{L_e-L_\tau}$ models, as shown in Fig. 2 by the navy blue shaded region.
- **LEP:** The coupling of Z' to electrons is strongly constrained by the measured cross-section for the processes $e^+e^- \rightarrow \ell^+\ell^-$ at the LEP-2 experiment [2]. For $M_{Z'} > \sqrt{s} = 209 \text{ GeV}$, we use the four-fermion contact interaction bounds, expressed as $g' \leq 0.044 M_{Z'}/(200 \text{ GeV})$ [125]. For $M_{Z'} < 209 \text{ GeV}$, the four-fermion description is no longer valid, and a conservative limit of $g' \leq 0.04$ is used [20]. These limits apply to the $U(1)_{L_e-L_\mu}$ and $U(1)_{L_e-L_\tau}$ models, as shown in Fig. 2 by the red shaded regions. For the $U(1)_{L_\mu-L_\tau}$ model, the LEP-1 measurement of the four-fermion final-state at the Z pole [126] was used to derive a constraint on Z' from $Z \rightarrow \mu^+\mu^-Z'$ decay, as well as from the universality of $Z \rightarrow e^+e^-$ and $Z \rightarrow \mu^+\mu^-$ [55], as collectively shown by the red curves in Fig. 2 bottom panel.

When the Z' couples to electrons, LEP-2 measurements of mono-photon events associated with large missing transverse energy at the Z pole [127, 128] can also be used to set stringent limits on the coupling of Z' to neutrinos. We show the mono-photon limits recast from Ref. [129] as the magenta shaded region.

- **LHC:** There exist dedicated searches for the Z' boson in the context of the $U(1)_{L_\mu-L_\tau}$ model by both ATLAS and CMS collaborations [130, 131] using the Z' production from the final-state radiation of μ or τ leptons in the Drell-Yan process. This is shown by the salmon (grey) shaded region for ATLAS (CMS) in Fig. 2, which is the most stringent limit to date in most of the searched mass ranges. The olive-dashed and brown-dashed curves are limit from 4ℓ search [132] and 3ℓ search [133] recast in Ref. [134].

A search based on $Z' \rightarrow \mu^+\mu^-$ has been performed by the LHCb collaboration (similar searches were also done by BABAR [135] and Belle [136]), which applies to the $U(1)_{L_e-L_\mu}$ and $U(1)_{L_\mu-L_\tau}$ models [137]. Similarly, Belle II has performed searches for the Z' boson using invisible Z' decays in $e^+e^- \rightarrow \mu^+\mu^-Z'$ [138] and also using visible Z' decay to $\tau^+\tau^-$ resonance in $e^+e^- \rightarrow \mu^+\mu^-\tau^+\tau^-$ [139]. These limits are applicable to the $U(1)_{L_\mu-L_\tau}$ case, but only for $M_{Z'} \lesssim 10 \text{ GeV}$, and hence, are not shown here.

Measurement of $\text{BR}(Z \rightarrow \mu^+\mu^-\tau^+\tau^-)$ by the CMS collaboration [140] will also be relevant for the $U(1)_{L_\mu-L_\tau}$ model; however, no limit on the Z' contribution has been set by this analysis. We have also checked that the constraint on the γ/Z - Z' kinetic mixing induced by the lepton loops [141, 142] from the direct $pp \rightarrow \ell^+\ell^-(\gamma)$ searches at the LHC [143] are rather weak and do not show up in the range of our interest in Fig. 2.

Even with so many existing studies of the $U(1)_{L_\alpha-L_\beta}$ gauge boson as listed above, a large parameter space is allowed around the electroweak scale and remains to be explored at future colliders, shown by the blank region in Fig. 2. We capitalize on this opportunity, and focus on the direct and indirect searches of the Z' boson at future lepton colliders to extend the sensitivity coverage to higher masses and/or smaller couplings.

III. Z' PHENOMENOLOGY AT FUTURE LEPTON COLLIDERS

In this section, we will explore the details of the Z' -boson phenomenology in the $U(1)_{L_\alpha-L_\beta}$ gauge model at future e^+e^- and $\mu^+\mu^-$ colliders. An earlier study of the $U(1)_{L_\mu-L_\tau}$ scenario exists

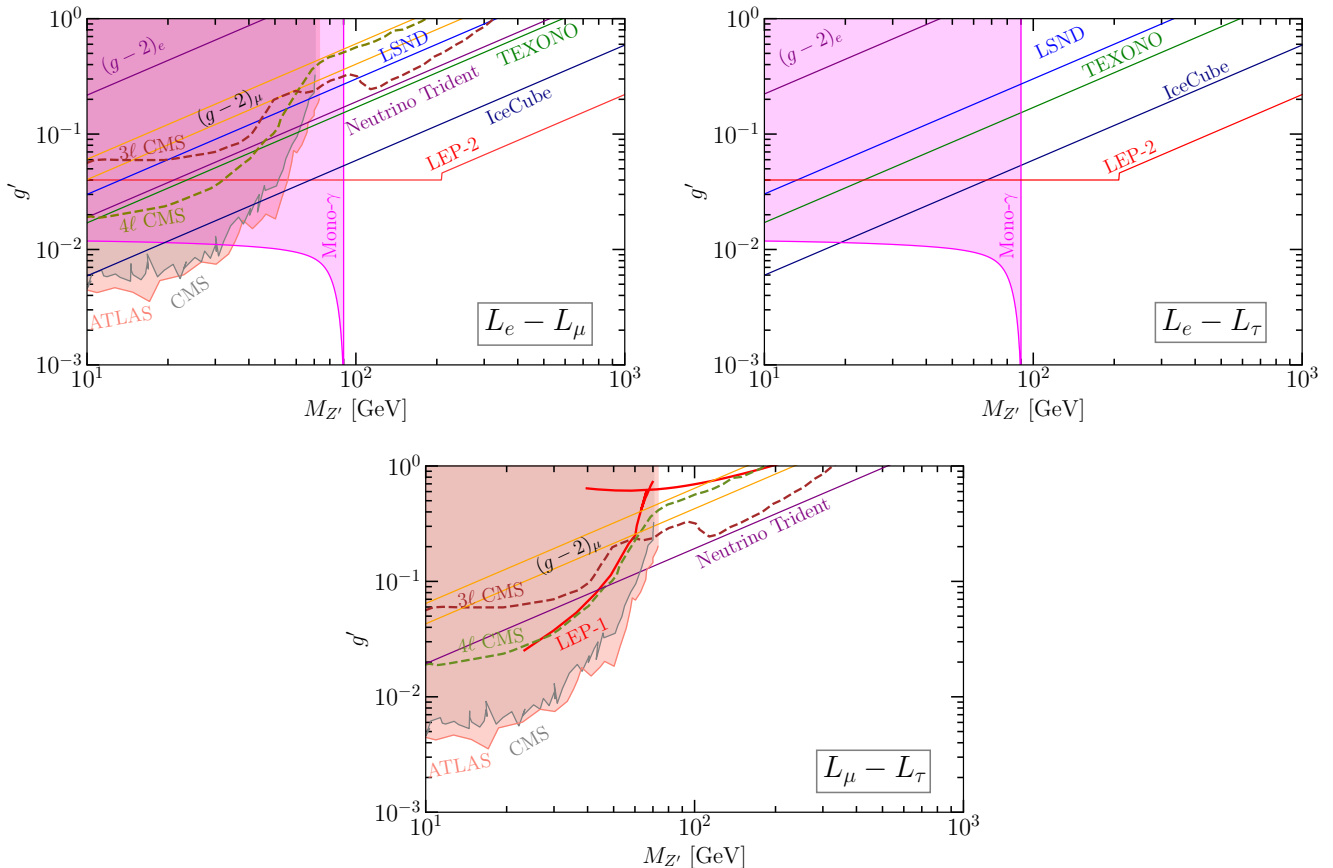


FIG. 2. Existing 95% CL exclusion bounds (except IceCube, which is at 90% CL) on the gauge boson mass $M_{Z'}$ and coupling g' in the $U(1)_{L_\alpha - L_\beta}$ models. See Section II B for details.

for a $\sqrt{s} = 3$ TeV muon collider [63]; see also Refs. [144–146] for related recent works. More careful considerations of the SM backgrounds, especially from the vector-boson fusion (VBF), will be examined in this work. In addition, we will extend our study to the $U(1)_{L_e - L_\mu}$ and $U(1)_{L_e - L_\tau}$ scenarios at both muon and electron-positron colliders. For concreteness and fair comparison, we will fix the center-of-mass energy at $\sqrt{s} = 3$ TeV for both electron [7] and muon [10] collider options, unless otherwise specified.

A. The Z' resonance production

A pronounced signal for Z' boson at a high-energy lepton collider can come from the direct lepton-pair annihilation, as shown in Fig. 3(a). Due to its short-lived nature in the parameter space of our interest [cf. Fig. 1], the Z' will decay promptly before entering the detector. In the beam-lepton decay channel, we have extra t -channel diagrams with Z' exchange, similar to the Bhabha scattering, as shown in Fig. 3(b). Two types of SM background will contribute to these dilepton final states. The first type comes from the same mechanism with annihilation or t -channel exchange but with the SM photon or Z boson. The second type comes from the lepton pair production through 2-to-4 processes, $\ell^+ \ell^- \rightarrow \ell'^+ \ell'^- + \ell^+ \ell^- (\nu \bar{\nu})$, in which the two forward/backward leptons are undetected, mainly induced by the neutral or charged current (NC or CC) VBF, as shown in Figs. 3(c) and 3(d). They can fake the signal for the case with large initial state radiation (ISR). We note that, the diboson production in Fig. 3(e) and the three-body production $\ell^+ \ell^- Z$ in Fig. 3(f), as well as many other crossing diagrams with $\ell^+ \ell^- + \nu \bar{\nu}$ final states, though potentially sizable, have rather different kinematics from the signal and can be effectively separated out, as we will comment on later.

The characteristic feature of the resonance signal is the invariant mass peak obtained via the

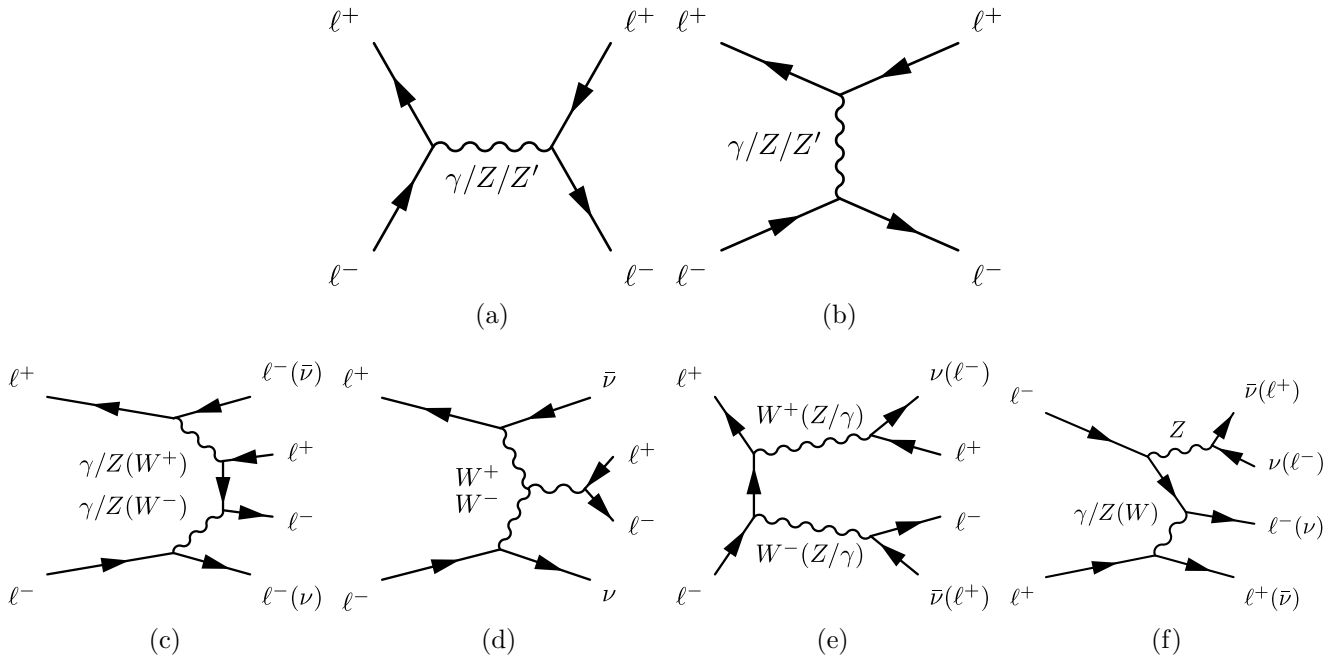


FIG. 3. Feynman diagrams for the lepton pair $\ell^+\ell^-$ production in the $U(1)_{L_{\alpha-L_{\beta}}}$ model (top row) and the representative vector-boson fusion or related backgrounds (bottom row) at high-energy lepton colliders.

single s -channel cross-section

$$\sigma(s, M_{Z'}) = \frac{g'^4}{12\pi} \frac{s}{(s - M_{Z'}^2)^2 + M_{Z'}^2 \Gamma_{Z'}^2}. \quad (12)$$

At the peak $s = M_{Z'}^2$, ignoring the interference and phase space acceptance, the rate is dominated by

$$\sigma(\sqrt{s} = M_{Z'}) = \frac{12\pi \text{Br}_i \text{Br}_f}{M_{Z'}^2}, \quad (13)$$

where $\text{Br}_{i(f)}$ is the Z' decay branching fraction to the initial (final) state i (f). In reality, the annihilation energy (the “partonic” collision energy $\sqrt{\hat{s}}$) is different from the designed collider energy (\sqrt{s}) due to the beam energy spread, and is typically lower mostly because of the ISR. Assuming a parton distribution function $f_{\ell}(x)$ for the contributing leptons with an energy fraction x , the observed cross-section at a given collider energy $\sqrt{s} > M_{Z'}$ is

$$\sigma(\sqrt{s}) = \int_0^1 dx f_{\ell}(x) \sigma(s, M_{Z'}) \approx 12\pi^2 \text{Br}_i \text{Br}_f \frac{\Gamma_{Z'}}{M_{Z'}^3} f_{\ell}(M_{Z'}^2/s), \quad (14)$$

where the narrow-width approximation (NWA) has been adopted with the on-shell condition

$$\hat{s} = xs \approx M_{Z'}^2. \quad (15)$$

In Fig. 4, we present the signal and background cross-sections for the lepton-pair production at high-energy electron and muon colliders in both the SM and the $U(1)_{L_{\alpha-L_{\beta}}}$ extended model, including the ISR effects for the resonance production. In the $U(1)_{L_{\alpha-L_{\beta}}}$ model, we fix $g' = 0.1$ and $M_{Z'} = 0.5/2/5$ TeV to demonstrate the features when the Z' mass is fully below the collider energy \sqrt{s} and when it is being crossed as \sqrt{s} increases. Here, on the left panel, we take the $e^+e^-/\mu^+\mu^- \rightarrow \tau^+\tau^-$ as representatives for the processes with final-state leptons different from initial-beam flavors, which probe the $U(1)_{L_e-L_{\tau}}$ and $U(1)_{L_{\mu}-L_{\tau}}$ models, respectively. The $U(1)_{L_e-L_{\mu}}$ can be probed with either $e^+e^- \rightarrow \mu^+\mu^-$ or $\mu^+\mu^- \rightarrow e^+e^-$ scatterings, which show similar behaviors as $e^+e^-/\mu^+\mu^- \rightarrow \tau^+\tau^-$, or via the Bhabha scatterings $e^+e^- \rightarrow e^+e^-$ and $\mu^+\mu^- \rightarrow \mu^+\mu^-$, as shown on the right panel. In the

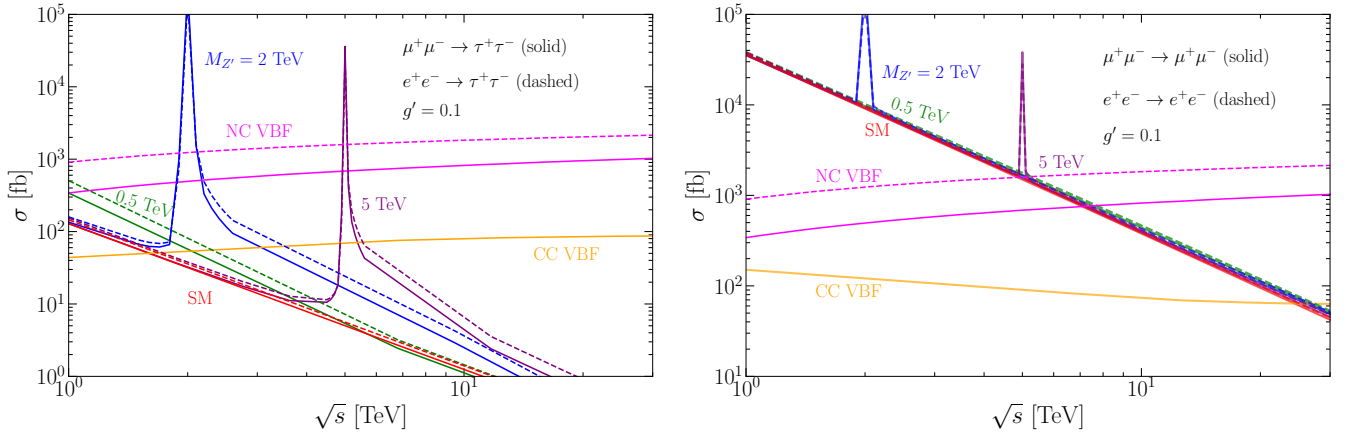


FIG. 4. Lepton-pair production cross-section versus the electron/muon collider energy in the SM and $U(1)_{L_{\alpha}-L_{\beta}}$ models. We take the $\tau^+\tau^-$ production as a representative for processes with final-state leptons different from initial beams on the left panel, while the one with the same initial- and final-state lepton flavors is shown on the right panel. The pre-selection cuts in Eq. (16) have been applied here.

rest of our simulation, we have imposed the universal pre-selection cuts (PSCs)

$$p_T^\ell > 30 \text{ GeV}, \quad |\eta_\ell| < 2.44, \quad \Delta R_{\ell\ell} > 0.3 \quad (16)$$

for final-state leptons, which are essential to regulate collinear divergence in the Bhabha scattering and to simulate the detector acceptance. The lepton pseudo-rapidity cut $|\eta_\ell| < 2.44$ corresponds to the detector coverage within $10^\circ < \theta < 170^\circ$. The signal cross-sections are calculated using WHIZARD [147, 148] and cross-checked using MadGraph [149], after interfacing with the UFO model files generated using FeynRules [150]. The QED ISRs are treated with WHIZARD, which resums soft photons to all orders and hard-collinear ones up to the third order [147, 148].

In Fig. 4, we see two types of behavior of the curves. The downward-going curves with the $1/s$ behavior correspond to the annihilation or regulated t -channel processes. The cross-section difference for the SM annihilation processes between the two panels is from the additional t -channel contributions in the same initial-final flavor case, $\ell^+\ell^- \rightarrow \ell^+\ell^-$ ($\ell = e, \mu$). When $\sqrt{s} \sim M_{Z'}$, we see a big enhancement in the lepton-pair cross-section due to the resonant production. Off the resonance when $\sqrt{s} > M_{Z'}$, there is still an enhancement peaked at $M(\ell^+\ell^-) \sim M_{Z'}$, due to the ISR, namely, the “radiative return” [151]. For $M_{Z'} \gg \sqrt{s}$ on the other hand, the first two diagrams in Fig. 3 both contribute to the signal, with the cross-section scaling as $\sigma \sim 1/M_{Z'}^2$.

In contrast, the upward-going curves in Fig. 4 indicate the NC and CC VBF processes, mediated by γ/Z and W bosons, respectively. The VBF backgrounds for both NC and CC are calculated with the WHIZARD fixed-order (FO) calculation. Since the photon-photon initiated processes dominate the NC contribution, we verified the above calculations with MadGraph’s equivalent photon approximation (EPA) [152], *i.e.*, improved Weizsacker-Williams approximation [153]. The VBF channels serve as a significant part of the SM background, in particular in the off-resonance region. With the collider energy at $\sqrt{s} = 3$ TeV of our interest, we see the VBF cross-section can even dominate the lepton-pair production, in both electron and muon collider scenarios. With respect to the NC VBF cross-sections for electron colliders, the muon ones are generally smaller, due to their large mass, which reduces the photon radiations. A similar situation occurs in the ISR annihilation cross-section as well. In comparison, the CC VBF cross-sections for the lepton pair production at electron and muon colliders are largely the same, as both lepton masses are negligible with respect to the W -boson one. We have also included the Higgs decay $H \rightarrow \tau\tau$, which yields about 27 fb at 30 TeV. The notable larger cross-section at lower energies in the second panel than in the first for CC VBF is owing to additional channels for the same initial- and final-state flavor, as well as the three-body contribution $\ell^+\ell^- \rightarrow \ell^+\ell^-Z$ in Fig. 3(f). As to be shown with optimization cuts later, these are only appreciable near the threshold for a heavy Z' . Although the backgrounds from 2-body [cf. Fig. 3(e)]

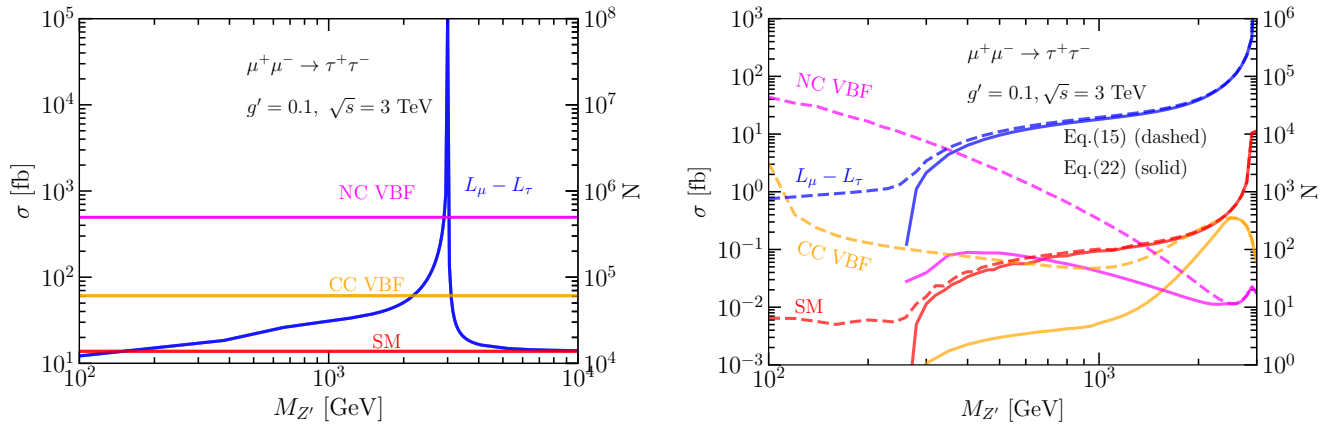


FIG. 5. Lepton-pair annihilation cross-sections versus the new gauge boson mass $M_{Z'}$ at a $\sqrt{s} = 3$ TeV muon collider. *Left*: With PSCs in Eq. (16). *Right*: With the optimization cuts $|M_{\tau\tau} - M_{Z'}| < 0.05 M_{Z'}$ (dashed curves), and in addition, $|y_{\tau\tau} \pm y_{Z'}| < 0.2$ (solid curves). We also include the number of events on the right y-axis, which corresponds to an integrated luminosity $\mathcal{L} = 1 \text{ ab}^{-1}$.

$U(1)_{L_{\mu}-L_{\tau}}$ $M_{Z'} [\text{TeV}]$	Signal			SM backgrounds		
	0.5	2	5	Annihilation	CC VBF	NC VBF
$\sigma [\text{fb}]$	$\mu^+\mu^- \rightarrow \tau^+\tau^-$					
Eq. (16)	22.5	50.9	15.0	13.8	61.3	510
$0.475 < M_{\ell\ell}/\text{TeV} < 0.525$	11.1			$5.86 \cdot 10^{-2}$	$6.48 \cdot 10^{-2}$	2.31
$1.59 < y_{\tau\tau} < 1.99$	9.6			$5.07 \cdot 10^{-2}$	$3.00 \cdot 10^{-3}$	$8.78 \cdot 10^{-2}$
$1.9 < M_{\ell\ell}/\text{TeV} < 2.1$		40.7		0.214	$2.10 \cdot 10^{-1}$	$2.49 \cdot 10^{-2}$
$0.20 < y_{\tau\tau} < 0.60$		39.1		0.205	$8.30 \cdot 10^{-2}$	$1.30 \cdot 10^{-2}$
$M_{\ell\ell} > 0.95\sqrt{s}$			11.0	11.0	$6.05 \cdot 10^{-2}$	$1.76 \cdot 10^{-2}$

TABLE II. The cut-flow table $\tau^+\tau^-$ pair production at a $\sqrt{s} = 3$ TeV muon collider. The gauge coupling is fixed at $g' = 0.1$.

and 3-body [cf. Fig. 3(f)] processes are sizable, they still fall below the SM s -channel contribution. Furthermore, they could be effectively separated from the signal by examining the large $p_T(\ell^+\ell^-)$ as opposed to $p_T(\ell^+\ell^-) \approx 0$ for the signal.

In the left panel of Fig. 5, we present the lepton-pair annihilation cross-sections versus the gauge boson mass $M_{Z'}$ in the $U(1)_{L_{\alpha}-L_{\beta}}$ model, with gauge coupling fixed as $g' = 0.1$, with the same cuts as in Fig. 4. We see that when $M_{Z'} < \sqrt{s}$, the cross-section increases while approaching the resonant energy. In contrast, for $M_{Z'} > \sqrt{s}$, we see the $U(1)_{L_{\alpha}-L_{\beta}}$ cross-section asymptotically approaches to the SM one, scaled as $\sigma \sim 1/M_{Z'}^2$, suggesting the limitation of the direct probe of heavy Z' at a lepton collider. In the right panel, we show the asymptotic behavior of the cross-sections when $\sqrt{s} \rightarrow M_{Z'}$, with the optimal cuts as labeled on the plot. In both panels, we also include the SM background cross-sections from the direct annihilation, as well as from the NC and CC VBF processes, for comparison.

We take $\mu^+\mu^- \rightarrow \tau^+\tau^-$ process as an example to probe the $U(1)_{L_{\mu}-L_{\tau}}$ model. Even with potentially larger SM background cross-sections, we can still hope to separate the Z' signal from the backgrounds based on their kinematic features. The normalized distributions of invariant mass $M_{\tau\tau}$ and rapidity $y_{\tau\tau}$ for the final-state lepton pairs, as well as the transverse momentum $p_T^{\tau^+}$ and cosine angle $\cos\theta_{\tau^+}$ for the positively-charged final-state lepton with respect to the e^+/μ^+ direction are shown in Fig. 6 for both signal and backgrounds, with PSCs in Eq. (16). For the $U(1)$ gauge model, we take $M_{Z'} = 500$ GeV and $g' = 0.1$ for demonstration.

For the $2 \rightarrow 2$ annihilation processes in the SM, the invariant mass is primarily peaked around the collision energy $M_{\tau\tau} = \sqrt{s}$, with a long tail at lower energies from the ISR. In contrast, for the

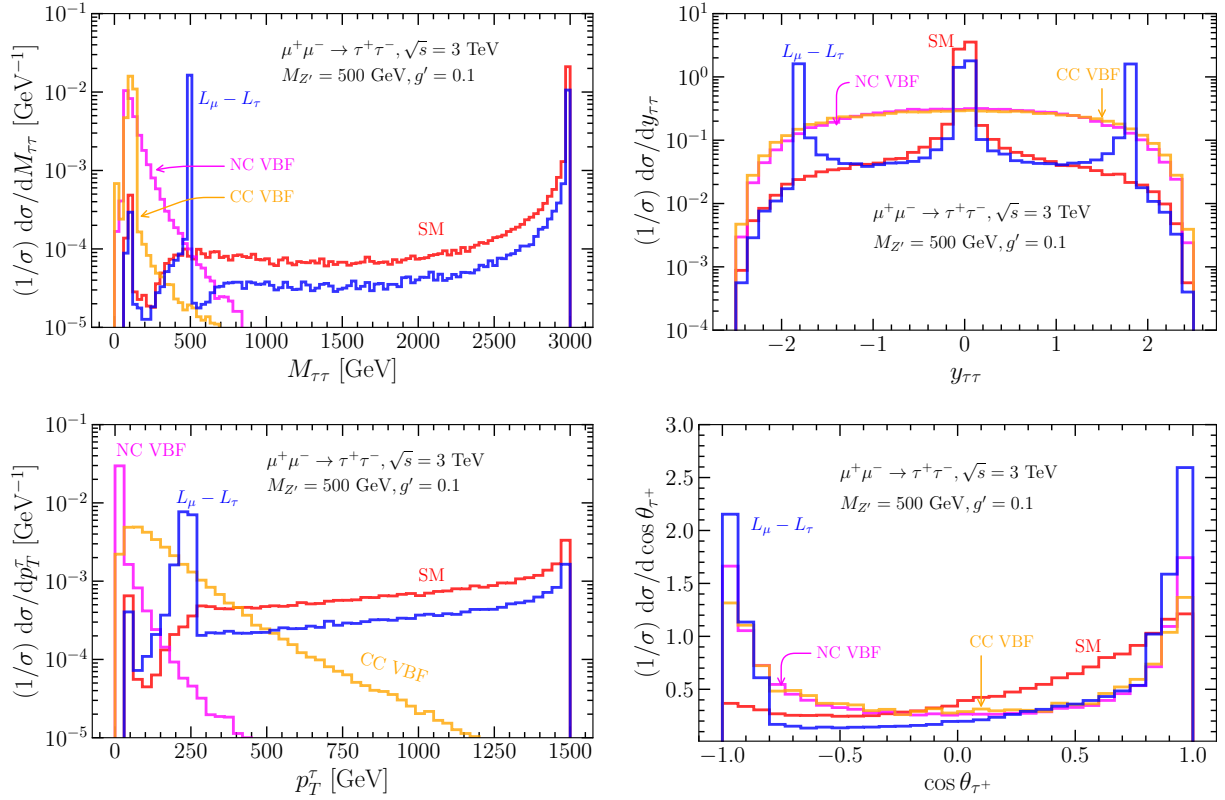


FIG. 6. Normalized kinematic distributions for the invariant mass $M_{\tau\tau}$ and rapidity $y_{\tau\tau}$ of the lepton pair, as well as the transverse momentum $p_T^{\tau^+}$ and angle cosine $\cos\theta_{\tau^+}$ of the positively-charged final-state τ lepton in the $\mu^+\mu^- \rightarrow \tau^+\tau^-$ scattering at a $\sqrt{s} = 3$ TeV muon collider. Here we have fixed $M_{Z'} = 500$ GeV and $g' = 0.1$ for the signal.

Z' signal, a resonance peak shows up at $M_{\tau\tau} = M_{Z'} < \sqrt{s}$ as a result of the so-called “radiative return”, indicating the potential to discover this new Z' particle, with the signal rate scaled as the coupling strength g'^2 . In comparison with the annihilation case, we see the distributions of the VBF channels, including both NC and CC, die out very quickly at the high invariant mass, as the parton luminosity decreases as $1/M_{\tau\tau}^2$. As such, the SM VBF backgrounds would possess less of a problem for a large $M_{Z'}$. We adopt an invariant mass selection cut to optimize the search for $M_{Z'}$ as

$$\begin{aligned} |M_{\ell\ell} - M_{Z'}| &< 0.05M_{Z'} \quad (10 \text{ GeV}) \quad \text{for resonance } M_{Z'} < \sqrt{s}; \\ M_{\ell\ell} &> 0.95\sqrt{s} \quad \text{for off shell } M_{Z'} \geq \sqrt{s}. \end{aligned} \quad (17)$$

for final-state tau (electron or muon) leptons, respectively. Here, the final-state tau requires a reconstruction from the tau decay products, in which case we consider a looser mass window as $0.05M_{Z'}$, while the final-state electrons and muons can be well observed in the detector, in which we take a 10 GeV mass window [7].

Another characteristic feature comes from the observation that the dominant configuration in the radiative return is from a leading single photon radiation. The kinematics can be determined through the 2-to-2 scattering process

$$\mu^+(p_1) + \mu^-(p_2) \rightarrow Z'(p_{Z'}) + \gamma(p_\gamma). \quad (18)$$

The final-state momenta can be parameterized in terms of the photon transverse momentum p_T and pseudo-rapidity η as

$$\begin{aligned} p_\gamma &= (p_T \cosh \eta, \vec{p}_T, p_T \sinh \eta), \\ p_{Z'} &= (\sqrt{s} - p_T \cosh \eta, -\vec{p}_T, -p_T \sinh \eta), \end{aligned} \quad (19)$$

where we have employed the momentum conservation $p_1 + p_2 = p_{Z'} + p_\gamma = (\sqrt{s}, \vec{0}, 0)$. With the on-shell condition $p_{Z'}^2 = M_{Z'}^2$, we obtain the photon transverse momentum as

$$p_T = \frac{s - M_{Z'}^2}{2\sqrt{s} \cosh \eta}. \quad (20)$$

The final-state Z' -boson rapidity can be analytically determined as

$$y(\eta) = \frac{1}{2} \log \frac{p_{Z'}^0 + p_{Z'}^3}{p_{Z'}^0 - p_{Z'}^3} = \frac{1}{2} \log \frac{se^\eta + M_{Z'}^2 e^{-\eta}}{se^{-\eta} + M_{Z'}^2 e^\eta}. \quad (21)$$

In the spirit of ‘‘radiative return’’ with a collinear photon, we have $|\eta| \rightarrow \infty$ (*i.e.*, $p_T \rightarrow 0$), the Z' rapidity becomes

$$|y(\pm\infty)| = y_{Z'} \equiv \log(\sqrt{s}/M_{Z'}). \quad (22)$$

In this case, the momentum fraction carried by the photon becomes

$$\bar{x} \equiv 1 - x = \frac{p_T \cosh \eta}{\sqrt{s}/2} \xrightarrow{|\eta| \rightarrow \infty} 1 - \frac{M_{Z'}^2}{s}, \quad (23)$$

while the beam lepton carries a fraction $x = M_{Z'}^2/s$, corresponding to the on-shell condition in Eq. (15). This is remarkable since it predicts the mono-chromatic value of the rapidity of Z' for a given mass at a fixed collider energy, which would single out the resonant signal over the continuum SM background. Examining the lepton-pair rapidity distribution in Fig. 6, we see in the annihilation processes that the 500 GeV Z' signal peaks at $|y_{\tau\tau}| = \log(\sqrt{s}/M_{Z'}) \approx 1.79$, whereas the SM contribution is primarily peaked around $y_{\tau\tau} \sim 0$, and the VBF processes are spread out. This motivates us to impose a rapidity selection cut, for a given hypothetical $M_{Z'}$,

$$|y_{\tau\tau} \pm y_{Z'}| < 0.2, \quad (24)$$

to increase the signal-to-background ratio further, which is shown on the right panel of Fig. 5 by the solid curves.

However, there is an additional complication. For $M_{Z'} \ll \sqrt{s}$, $y_{Z'} \approx \log \cot(\theta/2)$, which results in

$$\tan(\theta/2) \approx M_{Z'}/\sqrt{s}. \quad (25)$$

Assuming the minimal detector acceptance in the polar angle being about 10° ($|\eta_\ell| < 2.44$), then a particle of a mass $M < 0.088\sqrt{s}$ would mostly escape from the detection into the beam pipe, which leads to a missing particle of mass $M = (261, 872, 2615)$ GeV at a collider of $\sqrt{s} = (3, 10, 30)$ TeV. As a caveat, this rapidity optimization cut in Eq. (24) would not be applicable when $M_{Z'} < 0.088\sqrt{s}$ as $y_{Z'}$ goes beyond the detector acceptance.

In Table II, we demonstrate our cut-flow strategy with $g' = 0.1$ and $M_{Z'} = 0.5, 2$ and 5 TeV as examples. We see that the cuts are highly effective in preserving the signal. The cut on $M_{\ell\ell}$ is effective for both annihilation and VBF backgrounds, while that on $y_{\tau\tau}$ is more on reducing VBF background, by orders of magnitude. The cross-sections for both signal and backgrounds with optimization cuts $|M_{\ell\ell} - M_{Z'}| < 0.05M_{Z'}$ and subsequently $|y_{\ell\ell} \pm y_{Z'}| < 0.2$ (which only applies when $M_{Z'} > 261$ GeV) at a $\sqrt{s} = 3$ TeV muon collider are also shown in Fig. 5 (right panel).

B. Off-shell Z' production

When $M_{Z'} > \sqrt{s}$, the Z' resonance cannot be produced directly on-shell at a collider. However, the off-shell Z' -mediated diagrams, both in the s - and t -channels, as shown in Figs. 3(a) and 3(b) respectively, are expected to interfere with the SM ones, which yields a modification to the final-state lepton distribution with respect to the SM ones at the order of $s/M_{Z'}^2$. In such a way, an indirect

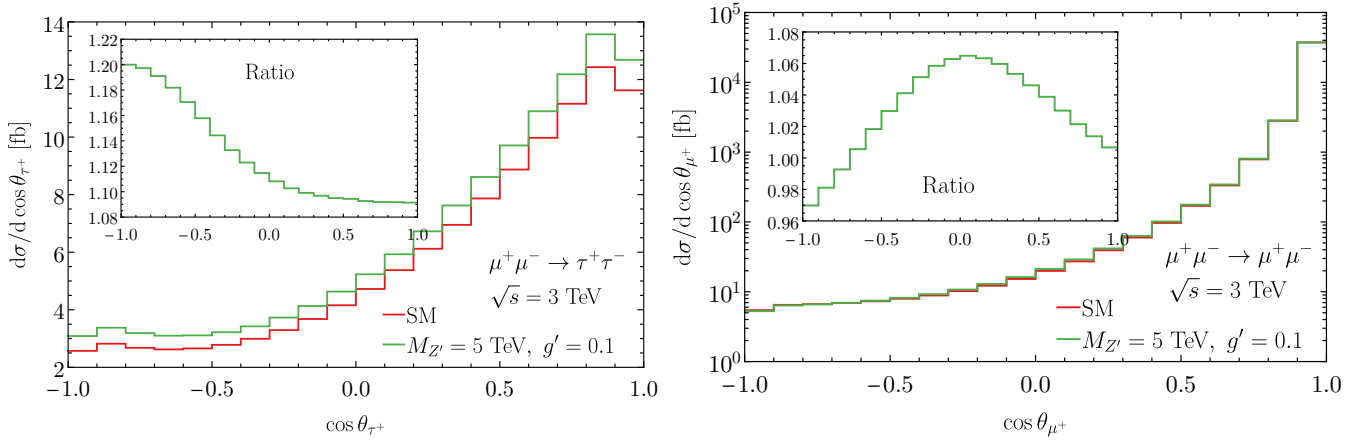


FIG. 7. The cosine angle distribution for the final-state leptons in the off-shell s -channel $\mu^+\mu^- \rightarrow \gamma/Z/Z' \rightarrow \tau^+\tau^-$ (left) and s/t -channel $\mu^+\mu^- \xrightarrow{\gamma/Z/Z'} \mu^+\mu^-$ (right) scatterings. The Z' signal comes from the difference between the SM and the Z' model, with the relative size of $(S+B)/B$ shown in the corresponding inset.

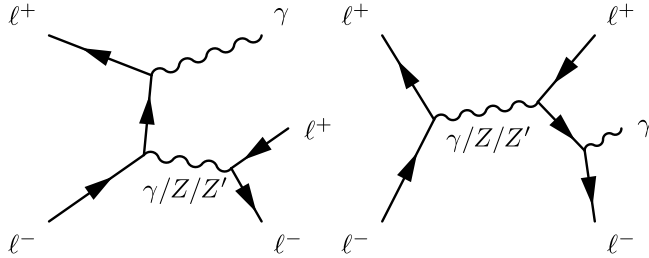


FIG. 8. Representative Feynman diagrams for lepton-pair production associated with a photon at a lepton collider.

sensitivity to the Z' boson can be placed based on precision measurements, *e.g.*, the forward-backward asymmetry (FBA). In Fig. 7, we show the cosine angle distributions of the final-state lepton in the s -channel $\mu^+\mu^- \rightarrow \gamma/Z/Z' \rightarrow \tau^+\tau^-$ and the s/t -channel $\mu^+\mu^- \xrightarrow{\gamma/Z/Z'} \mu^+\mu^-$ processes, with the benchmark values of $M_{Z'} = 5$ TeV and $g' = 0.1$, and with the same pre-selection cuts as in Eq. (16). We see that in the s -channel scattering $\mu^+\mu^- \rightarrow \tau^+\tau^-$, the additional Z' mediated process not only changes the shape of angle distribution, but also enhances the total rate. In the Bhabha-like scattering $\mu^+\mu^- \rightarrow \mu^+\mu^-$, the total rate largely remains unchanged, mainly due to the dominant t -channel γ -mediated background, while the FBA gets modified. Later, we will perform a bin-by-bin angular distribution analysis in both cases, which implicitly includes the FBA information.

C. $Z' + \gamma$ associated production

In the ISR for the resonance production as explored above, the soft or collinear photons are unobservable in the detector. In contrast, a radiated photon can be detected as long as it is within the acceptance of the electromagnetic calorimeter. We show the corresponding Feynman diagrams in Fig. 8, including channels with the same or different initial- and final-state lepton flavors. Different from the channels in Fig. 3, the resolved photon here requires additional acceptance, which we choose as

$$p_T^\gamma > 30 \text{ GeV}, \quad |\eta_\gamma| < 2.44, \quad \Delta R_{\gamma\ell} > 0.3, \quad (26)$$

on top of the PSCs in Eq. (16). Although the total signal rate will be smaller due to the additional hard photon radiation, the unique kinematics may help signal identification and property studies.

In Fig. 9, we show the cross-sections for the $Z' + \gamma$ production with both signal and SM backgrounds with the pre-selection cuts in Eq. (16) plus Eq. (26). As before, the signal and SM annihilation cross-

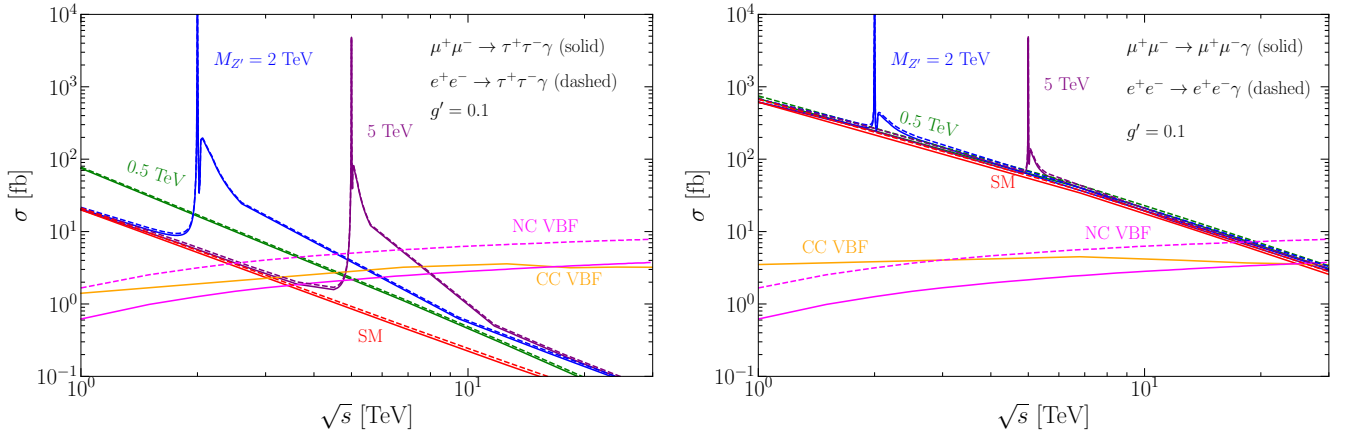


FIG. 9. The cross-sections for $e^+e^-/\mu^+\mu^- \rightarrow \tau^+\tau^-\gamma$ (left) and $e^+e^-(\mu^+\mu^-) \rightarrow e^+e^-(\mu^+\mu^-)\gamma$ (right).

$U(1)_{L_\mu-L_\tau}$	Signal			SM		
$M_{Z'}$ [TeV]	0.5	2	5	Annihilation	CC VBF	NC VBF
σ [fb]	$\mu^+\mu^- \rightarrow \tau^+\tau^-\gamma$					
Eqs. (16) and (26)	8.37	14.6	5.26	4.93	2.29	1.14
$0.475 < M_{\ell\ell}/\text{TeV} < 0.525$	3.95			$2.16 \cdot 10^{-2}$	$6.95 \cdot 10^{-3}$	$4.85 \cdot 10^{-2}$
$1.9 < M_{\ell\ell}/\text{TeV} < 2.1$		10.4		$6.95 \cdot 10^{-2}$	$1.21 \cdot 10^{-2}$	$2.70 \cdot 10^{-3}$
$M_{\ell\ell} > 0.95\sqrt{s}$			1.14	0.40	$2.50 \cdot 10^{-5}$	$1.08 \cdot 10^{-3}$

TABLE III. The cut-flow table for $\tau^+\tau^-\gamma$ pair production at a $\sqrt{s} = 3$ TeV muon collider. The gauge coupling is fixed at $g' = 0.1$.

sections are calculated with WHIZARD and cross-checked with MadGraph. The NC VBF is taken with the MadGraph EPA, while the CC VBF is done with the WHIZARD FO calculation. Similar to the direct Z' production via ISR in the last section, there is a sharp peak around $\sqrt{s} \approx M_{Z'}$, as a result of the resonant production and decay of $Z' \rightarrow \ell^+\ell^-\gamma$. We also get notable resonance enhancements when $\sqrt{s} \gtrsim M_{Z'}$, while the additional resolved photon requires a slightly larger collider energy $\sqrt{s} \sim E_{Z'} + E_\gamma$. Different from the direct production channel, we see the VBF cross-sections, as well as the other higher-order diagrams $W^+W^-\gamma$, $ZZ\gamma$, are significantly suppressed, as a result of both one additional electric gauge coupling and the photon selection cuts. As a result, the SM background mainly comes from the diagrams in Fig. 8 with a γ/Z mediation.

In Fig. 10 (left), we show the $Z' + \gamma$ cross-section at a 3 TeV muon collider as a function of the Z' mass, with the gauge coupling fixed at $g' = 0.1$. We have used the PSCs in Eq. (16) together with Eq. (26). In comparison with the single Z' production in Fig. 5, the $Z' + \gamma$ cross-section gets reduced by about one order of magnitude, with a similar situation to the SM annihilation background. The NC/CC VBF backgrounds get a two/one-order of magnitude reduction.

In Fig. 11, we show the distributions of the lepton-pair invariant mass $M_{\tau\tau}$, rapidity $y_{\tau\tau}$, the cosine angle of the τ^+ , as well as the transverse momentum for τ^+ and photon γ , with $M_{Z'} = 500$ GeV for demonstration. As before, we get resonance peak at $M_{\tau\tau} = M_{Z'}$, which motivates an optimization cut $|M_{\tau\tau} - M_{Z'}| < 0.05M_{Z'}$, with the cut efficiency shown in Table III, and signal and background cross-sections shown in Fig. 10 (right). Meanwhile, we also see minor side peaks in the rapidity distributions around $|y(\eta)| \sim 1.67$, which can be directly read from Eq. (21) with the boundary condition $|\eta| = 2.44$. But the spreading is much wider than the inclusive Z' channel, due to the hard photon recoiling.

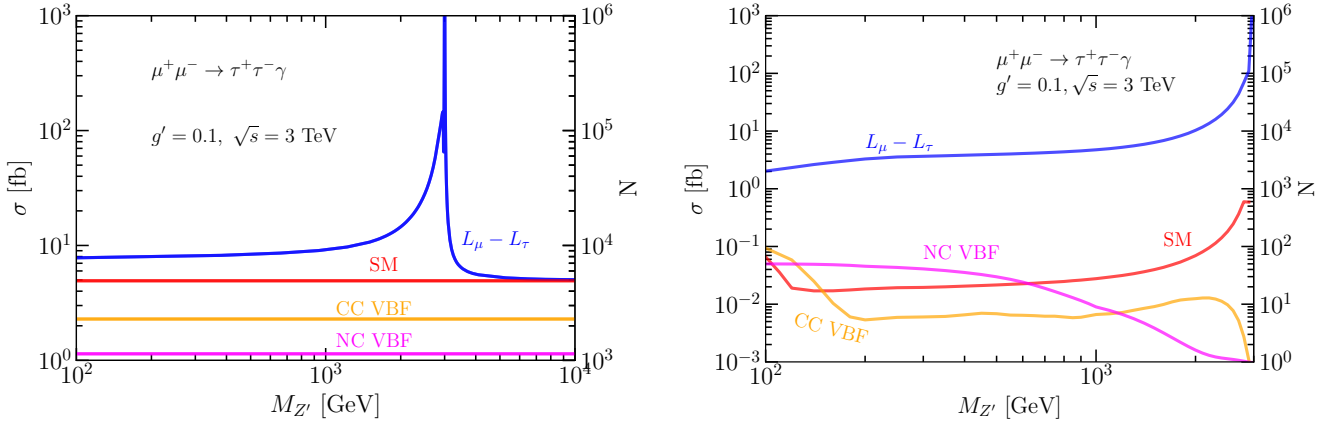


FIG. 10. *Left*: The pre-selection cross-section of $\tau\tau + \gamma$ associated production versus the Z' -boson mass $M_{Z'}$ at a 3 TeV muon collider. *Right*: The same cross-section, but with additional invariant mass cut $|M_{\tau\tau} - M_{Z'}| < 0.05M_{Z'}$.

$U(1)_{L_\mu - L_\tau}$	Signal			SM
$M_{Z'} [\text{TeV}]$	0.5	2	5	Annihilation
$\sigma [\text{fb}]$	$\mu^+\mu^- \rightarrow \nu\bar{\nu}\gamma$			
$ \eta_\gamma < 2.44, p_T^\gamma > 30 \text{ GeV}$	$1.61 \cdot 10^3$	$1.62 \cdot 10^3$	$1.60 \cdot 10^3$	$1.61 \cdot 10^3$
$0.475 < M_{\text{recoil}}/\text{TeV} < 0.525$	7.00			0.39
$1.9 < M_{\text{recoil}}/\text{TeV} < 2.1$		38.6		22.5
$M_{\text{recoil}} > 0.95\sqrt{s}$			837	839

TABLE IV. The cut-flow table for mono-photon production at a $\sqrt{s} = 3 \text{ TeV}$ muon collider. The gauge coupling is fixed at $g' = 0.1$.

D. Mono-photon final state

For the model under consideration, besides the charged-lepton channels, the Z' can also decay into neutrinos, with the corresponding flavors. Although this decay mode will result in missing momentum, the additional photon radiation, as shown in Fig. 12, will help to trigger the events and reconstruct the missing mass.

We can take advantage of the “recoil mass” [154] defined as

$$M_{\text{recoil}}^2 = (p_1 + p_2 - p_\gamma)^2 = s - 2\sqrt{s}E_\gamma. \quad (27)$$

For the on-shell Z' production, the photon energy will be monochromatic and the recoil mass will lead to a mass peak at the Z' resonance, in spite of the Z' decay final states.

Similarly as before, the pre-selection cuts as Eq. (26) together with $M_{\text{recoil}} = M_{\nu\bar{\nu}} > 150 \text{ GeV}$ (to remove the on-shell $Z \rightarrow \nu\bar{\nu}$ background) are imposed. The photon energy is monochromatic near $E_\gamma = (s - M_{Z'}^2)/2\sqrt{s} \approx 1460 \text{ GeV}$ for $M_{Z'} = 500 \text{ GeV}$. Thus, the missing neutrinos lead to the recoil mass, as the reconstructed resonance peak around $M_{\text{recoil}} = M_{Z'}$. Based on this observable, we can optimize the signal-background ratio with an additional cut $|M_{\text{recoil}} - M_{Z'}| < 10 \text{ GeV}$, with the efficiency demonstrated in Table IV. The cross-sections for the signal and background are shown in Fig. 13.

E. Four-lepton final states

The discussions thus far rely on the fact that the Z' couples to the initial e^\pm or μ^\pm beam particles at a collider. In the scenario that the Z' does not have coupling to the initial beam particles, it

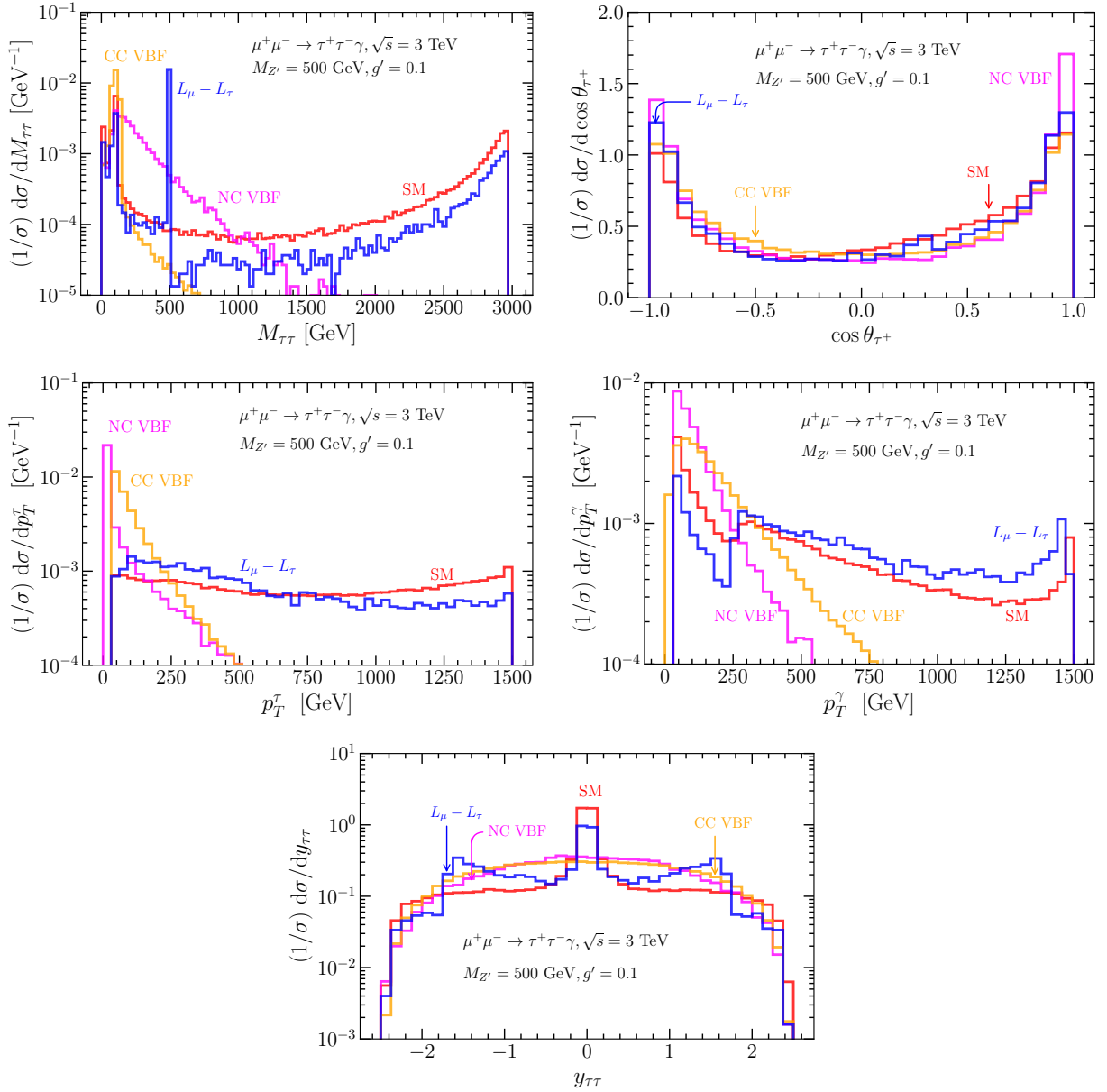


FIG. 11. The distributions $\cos\theta_{\tau^+}$, $p_T^{\tau^+}$, $M_{\tau\tau}$ and p_T^γ in the $\mu^+\mu^- \rightarrow \tau^+\tau^-\gamma$ scattering process at a 3 TeV muon collider with PSCs, Eq. (16) and Eq. (26).

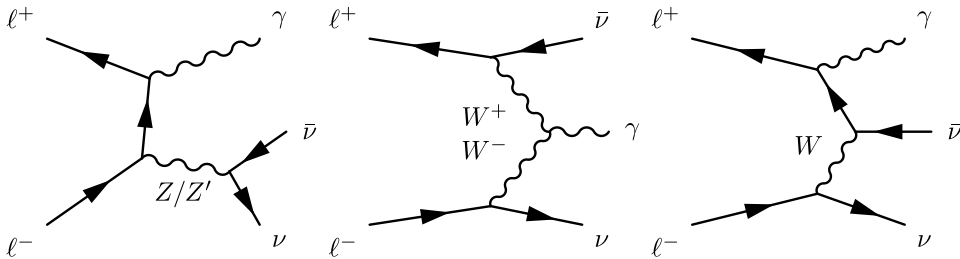


FIG. 12. Feynman diagrams for the mono-photon signal and background at a high-energy lepton collider.

can still be produced through the radiation of the final-state particle, as shown in Fig. 14. Take the $U(1)_{L_\mu-L_\tau}$ model at an e^+e^- collider as an example. The signal processes under consideration come from

$$e^+e^- \rightarrow \mu^+\mu^-Z', \tau^+\tau^-Z' \rightarrow \mu^+\mu^-\mu^+\mu^-, \mu^+\mu^-\tau^+\tau^-, \tau^+\tau^-\tau^+\tau^-. \quad (28)$$

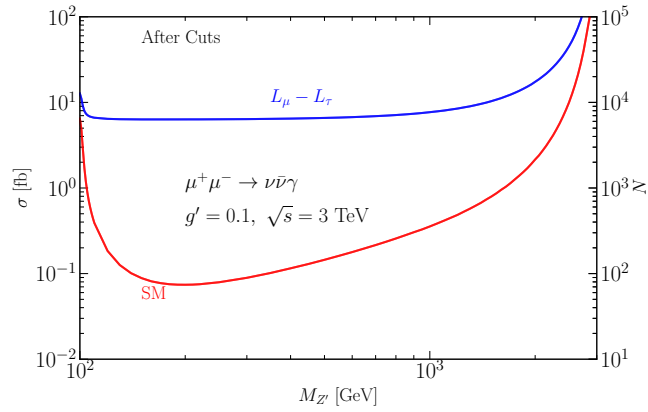


FIG. 13. The cross-sections for the mono-photon signal $\mu^+\mu^- \rightarrow \nu\bar{\nu}\gamma$ and SM background with cuts in Eq. (26) and $|M_{\text{recoil}} - M_{Z'}| < 10$ GeV.

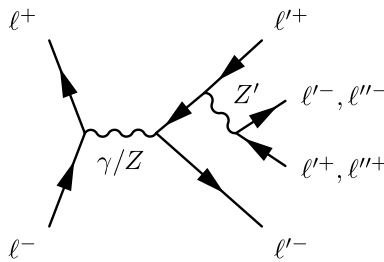


FIG. 14. Feynman diagrams for four-lepton production via Z' (which does not couple to the beam particles).

In comparison with the scenario where Z' directly couples to the initial beam particle, the sensitivity is expected to be much weaker, as a result of the smaller production cross-section and relatively higher SM background. As before, we take Eq. (16) as pre-selection cuts and optimize with an invariant mass cut $|M_{\ell\ell} - M_{Z'}| \leq 10$ GeV for electron/muon ($0.05M_{Z'}$ for τ) pairs to present the sensitivity projections. We note that the leading SM background is from $e^+e^- \rightarrow ZZ(\gamma^*\gamma^*) \rightarrow \ell^+\ell^-\ell^+\ell^-$. Thus we can significantly enhance the signal sensitivity by removing this Z/γ^* contribution with a cut $M(\ell^+\ell^-) > 150$ GeV for the lepton pair, which may be lowered and adjusted when very close to the threshold.

In fact, there are other contributions with Z' radiating off the final state neutrinos: $e^+e^- \rightarrow Z^* \rightarrow \nu\bar{\nu}Z' \rightarrow \nu\bar{\nu}\tau^+\tau^-$. Similarly, we could further improve the sensitivity by including the additional decay channels $Z' \rightarrow \nu_\mu\bar{\nu}_\mu, \nu_\tau\bar{\nu}_\tau$. One could utilize the recoil mass variable from the accompanying charged leptons to reconstruct the Z' resonant signal in this invisible decay mode. However, we expect such a larger background in the missing neutrino channels that we will not perform a comprehensive analysis here.

F. Sensitivity summary

Now we will combine the sensitivities from all the channels discussed above and will summarize our results for the direct and indirect searches of the leptophilic Z' model at high-energy lepton colliders.

For the direct on-shell Z' resonance production, we use the statistical significance metric

$$\mathcal{S} = \frac{S}{\sqrt{S + B + \delta^2(S + B)^2}}, \quad (29)$$

and use $\mathcal{S} = 2$ as the 2σ sensitivity limit (equivalent to 95% CL) in presenting our projections. Here,

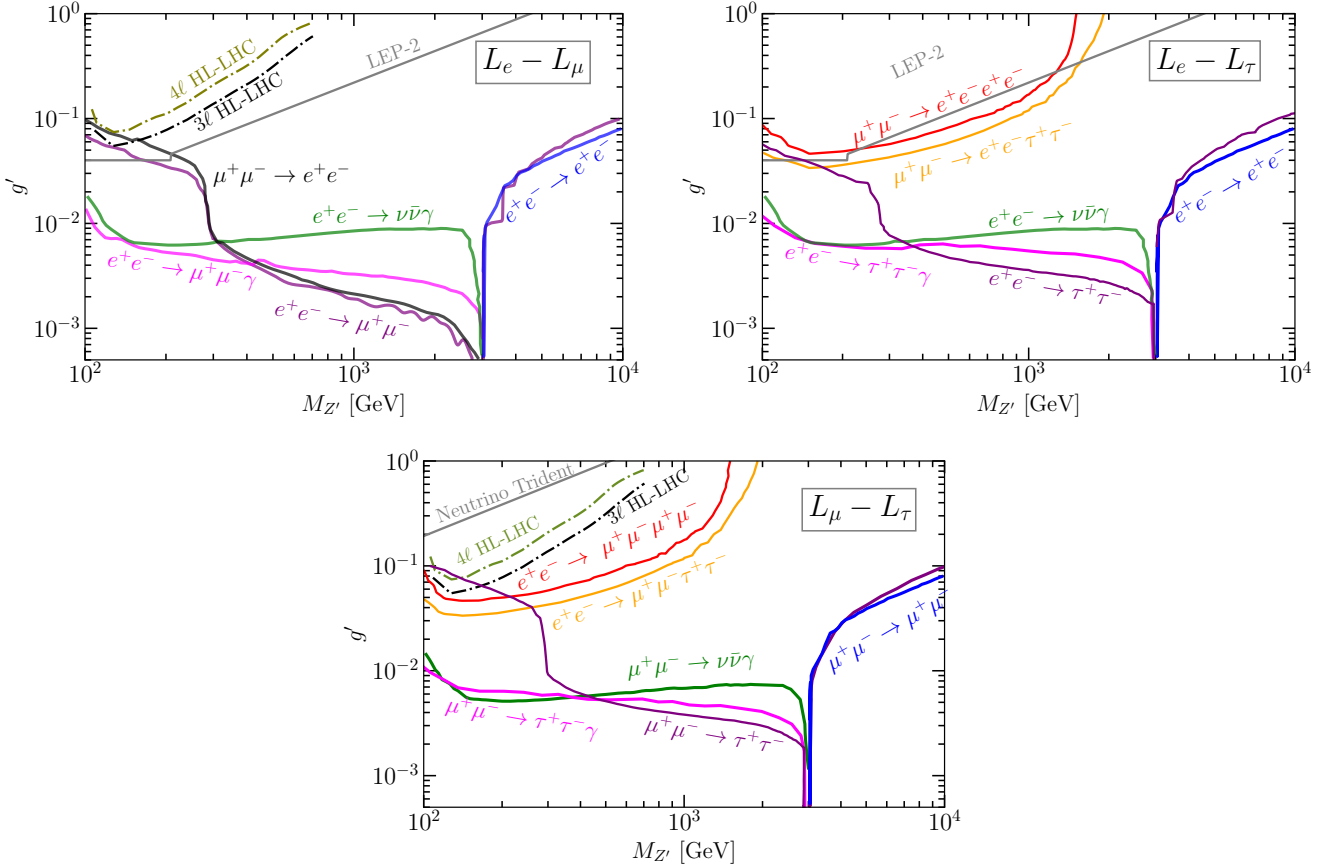


FIG. 15. The 95% CL sensitivity for the $U(1)_{L_\alpha-L_\beta}$ models at $\sqrt{s} = 3$ TeV electron and muon colliders. The grey-shaded regions show the current exclusion limits [cf. Fig. 2]. We have also shown the projected sensitivity from $pp \rightarrow 3\ell/4\ell$ at HL-LHC [158] by the black/green dot-dashed curves.

the systematic uncertainty is assumed to be $\delta = 0.1\%$ [154]. The S and B correspond to the signal and background events, respectively:

$$\begin{aligned} S &= N^{\text{SM}+Z'} - N^{\text{SM}} = \varepsilon \mathcal{L} (\sigma^{\text{SM}+Z'} - \sigma^{\text{SM}}), \\ B &= N^{\text{SM}} = \varepsilon \mathcal{L} \sigma^{\text{SM}}, \end{aligned} \quad (30)$$

with ε as the reconstruction efficiency. For illustration, we take a $\sqrt{s} = 3$ TeV electron/muon collider with an integrated luminosity of $\mathcal{L} = 1 \text{ ab}^{-1}$. For electron and muon final states, the reconstruction efficiency can reach above 95% at lepton colliders [155], and even close to 100% [7]. In comparison, the tau identification efficiency can reach above 70% [156] (and potentially 80% [157]) at lepton colliders. In this work, we follow the treatment in Ref. [63] to apply $\varepsilon_{e,\mu} = 100\%$ detection efficiency for electron and muon final-state events, while $\varepsilon_\tau = 70\%$ for the final-state tau events, in addition to the larger invariant mass window cut as in Eq. (17).

For the indirect off-shell Z production with $M_{Z'} > \sqrt{s}$, we take the cosine angle distribution with 20 even bins, as shown in Fig. 7. We perform a bin-by-bin analysis with the χ^2 -sensitivity defined as

$$\chi^2 = \sum_i \frac{S_i^2}{S_i + B_i + \delta^2 (S_i + B_i)^2}, \quad (31)$$

where S_i and B_i respectively indicate the corresponding signal and background events in the i^{th} bin. We then use $\chi^2 = 4$ to obtain the 95% CL sensitivity limit.

The electron and muon collider sensitivities to the leptophilic Z' models are summarized in Fig. 15 for $\sqrt{s} = 3$ TeV with the optimal cuts discussed above. The general features for the on-shell and

off-shell probes of the Z' parameter space are very similar, with the main difference arising from the tau final-state cut and sub-dominant differences from electron/muon beam mass effect and tau reconstruction efficiency with respect to the electron/muon ones.

In each of the three cases of $U(1)_{L_\alpha-L_\beta}$, the strongest probe at large Z' mass, *i.e.*, $M_{Z'} \gtrsim 300$ GeV, comes from the lepton pair production through direct on-shell resonance decay with ISR, which reaches sensitivities down to $g' \sim 10^{-3}$ when $M_{Z'} \sim \sqrt{s} = 3$ TeV. The $U(1)_{L_e-L_\mu}$ model incorporates the best sensitivity among these three models, while the $U(1)_{L_e-L_\tau}$ sensitivity is slightly less due to the lower tau reconstruction efficiency, and the $U(1)_{L_\mu-L_\tau}$ sensitivity is further reduced because of the additional signal suppression from the ISR owing to the larger muon mass. In the low Z' mass regime, the lepton-pair channel loses the constraining power because of two factors: First, the VBF background, especially the NC one, takes over in the low mass region. Second, we have employed a rapidity optimization cut $|y_{\ell\ell} \pm y_{Z'}| < 0.2$, where $y_{Z'} = \log(\sqrt{s}/M_{Z'})$, to improve the signal-to-background ratio, which loses effectiveness, when the $y_{Z'}$ goes beyond the detector acceptance. As a consequence, the $\ell^+\ell^-\gamma$ associated production channel takes over in this regime, which was also observed in Ref. [63]. In this regime, the mono-photon channel $\nu\bar{\nu}\gamma$ with the recoil mass can reach a similar sensitivity as shown in Fig. 15. In comparison between the electron and muon beams, the muon collider gets a slightly better sensitivity, due to the lower SM background induced by the larger muon mass in the photon radiation as Fig. 12 shown. A similar situation happens to the photon associated production channel as well.

When $M_{Z'}$ goes above the collider energy \sqrt{s} , the resonance Z' can be only produced off-shell. We have applied a bin-by-bin analysis based on the final-state angular distributions for both s - and t -channel processes, which provides an indirect probe to the Z' coupling around $10^{-2} \sim 10^{-1}$ up to $M_{Z'} < 10$ TeV, which improves upon the existing LEP contact interaction bound by roughly two orders of magnitude. In general, we see that the t -channel Bhabha scattering gives a stronger probe than the s -channel annihilation, due to the modification of the FBA as shown in Fig. 7. The τ final state, which can be only produced through the s channel, gives a slightly worse sensitivity, as a consequence of the lower reconstruction efficiency than electrons and muons.

In the scenario that the gauge boson Z' does not couple to the initial beam leptons, *e.g.*, for the $U(1)_{L_\mu-L_\tau}$ Z' search at the electron collider, we focus on the four-lepton production channel, which can potentially produce the Z' boson through the final-state radiation, *e.g.*, $e^+e^- \rightarrow \mu^+\mu^-(Z' \rightarrow \mu^+\mu^-/\tau^+\tau^-)$. A similar analysis based on the signal-to-background ratio has been performed, which shows a weaker sensitivity, around $5 \times 10^{-2} \sim 1$ for $100 \text{ GeV} < M_{Z'} \lesssim 1 \text{ TeV}$, as shown in Fig. 15. It is driven by the smaller production rate, as well as a relatively larger SM background.

To summarize, in comparison with the existing constraints, the future high-energy lepton colliders provide a great potential to probe extended regions of the leptophilic Z' parameter space for $M_{Z'} > M_Z$.

IV. GRAVITATIONAL WAVE SIGNAL

As alluded to in Section I, the $U(1)$ -extended gauge model, if classically conformal or scale-invariant, guarantees the phase transition associated with its spontaneous breaking to be strongly first-order, and thus may lead to an observable GW signal [159–167]. The GW signal is not only complementary to the searches at future lepton colliders discussed above, but can also probe an extended $(M_{Z'}, g')$ parameter space well beyond the reach of colliders. In this section, we explore the predictions for the GW signal in the conformal $U(1)_{L_\alpha-L_\beta}$ models, and show the complementarity with the collider constraints discussed above. For technical details of the formalism to compute the GW spectrum from strong first-order phase transition (SFOPT), see *e.g.* Ref. [168].

A. Effective potential and thermal corrections

Imposing the classically conformal invariance, the tree-level scalar potential at zero temperature is given as

$$V_{\text{tree}} = \lambda_H (H^\dagger H)^2 + \lambda (\Phi^\dagger \Phi)^2 - \lambda' (\Phi^\dagger \Phi) (H^\dagger H), \quad (32)$$

where H is the SM Higgs doublet, $\Phi = (\phi + iG)/\sqrt{2}$ is an SM-singlet complex scalar field which is responsible for the $U(1)$ -symmetry breaking (see Table I), and we have assumed $\lambda_H, \lambda, \lambda' > 0$. The quadratic mass terms (like $\mu_H^2 H^\dagger H$) are absent in Eq. (32) due to the conformal invariance. In this case, the $U(1)$ symmetry breaking is achieved radiatively, *i.e.*, a non-zero VEV of Φ , $\langle \Phi \rangle = v_\Phi/\sqrt{2}$, arises purely from the renormalization group (RG) running of the quartic coupling λ , as in the original Coleman-Weinberg model [29]. This consequently gives mass to the $U(1)$ gauge boson, $M_{Z'} = 2g'v_\Phi$, as well as the tree-level mass term for the SM Higgs boson through the quartic term λ' , *i.e.* $m_h^2 = \lambda'v_\Phi^2 = 2\lambda_H v^2$ [31, 32]. The negative sign in the last term of Eq. (32) ensures that the induced squared mass for the Higgs doublet is negative, and the electroweak symmetry breaking is driven in the same way as in the SM.

For $v_\Phi \gg v$, the symmetry breaking occurs first along the ϕ direction. Following the Gildener-Weinberg approach [169], the zero-temperature effective potential for ϕ can be written as [170, 171]

$$V_0(\phi, t) = \frac{1}{4} \lambda(t) [G(t)]^4 \phi^4, \quad (33)$$

where $t = \log(\phi/\mu)$, with μ being the renormalization scale, and

$$G(t) = \exp \left[- \int_0^t dt' \gamma(t') \right]. \quad (34)$$

The anomalous dimension in the Landau gauge⁴ is given by

$$\gamma(t) = \frac{-a_2}{32\pi^2} g'^2(t), \quad (35)$$

with $a_2 = 24$ [31, 177]. The gauge coupling strength $\alpha_{g'} = g'^2/4\pi$ and quartic coupling strength $\alpha_\lambda = \lambda/4\pi$ obey the following RG equations

$$2\pi \frac{d\alpha_{g'}}{dt} = b\alpha_{g'}^2(t), \quad 2\pi \frac{d\alpha_\lambda(t)}{dt} = a_1\alpha_\lambda^2(t) + 8\pi\alpha_\lambda(t)\gamma(t) + a_3\alpha_{g'}^2(t), \quad (36)$$

where $b = 16/3$, $a_1 = 10$, and $a_3 = 48$ [31].⁵ Setting the renormalization scale μ to be the VEV v_Φ at the potential minimum $\phi = v_\Phi$ (*i.e.* $\mu = v_\Phi$), or equivalently, $t = 0$, the stationary condition

$$\left. \frac{dV}{d\phi} \right|_{\phi=v_\Phi} = \frac{e^{-t}}{v_\Phi} \left. \frac{dV}{dt} \right|_{t=0} = 0, \quad (37)$$

leads us to the relation

$$a_1\alpha_\lambda^2(0) + a_3\alpha_{g'}^2(0) + 8\pi\alpha_\lambda(0) = 0. \quad (38)$$

Thus $\alpha_\lambda(0)$ can be determined by $\alpha_{g'}(0)$, and therefore, the scalar sector has only two free parameters, v_Φ and $\alpha_{g'}(0)$, which can be traded for the gauge boson mass $M_{Z'}$ and the gauge coupling g' evaluated at $\mu = v_\Phi$. One can then analytically solve the running of the couplings, and hence, the scalar potential [31]:

$$V_0(\phi, t) = \frac{\pi\alpha_\lambda(t)}{\left(1 - \frac{b}{2\pi}\alpha_{g'}(0)t\right)^{a_2/b}} \phi^4. \quad (39)$$

⁴ The issues concerning the gauge-dependence and impact on GW predictions have been addressed in Refs. [172–176].

⁵ We have checked using SARAH [178] that only the value of b is different for the $U(1)_{L_\alpha - L_\beta}$ case from the $U(1)_{B-L}$ case.

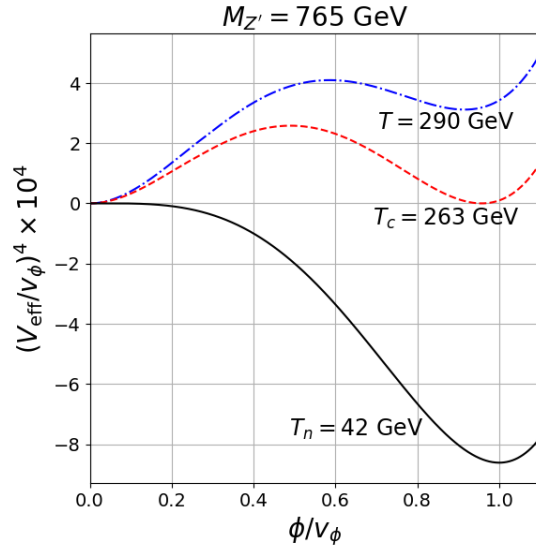


FIG. 16. Effective potential at different temperatures $T > T_c$ (dot-dashed), $T = T_c$ (dashed) and $T = T_n$ (solid), for a fixed $M_{Z'} = 765$ GeV.

As for the finite-temperature effects on the effective scalar potential, since the time evolution has two scales in it, ϕ and T (with T being the temperature of the Universe), we replace the renormalization scale parameter t with $u = \log(\Lambda/v_\Phi)$, where $\Lambda = \max(\phi, T)$ represents the largest energy scale in the system. The finite-temperature, one-loop effective potential is then given by

$$V_{\text{eff}}(\phi, T) = V_0(\phi, u) + V_T(\phi, T) + V_{\text{daisy}}(\phi, T), \quad (40)$$

where V_0 is given by Eq. (39), and V_T is the thermal contribution from bosonic one-loop [159]:

$$V_T(\phi, T) = \frac{3T^4}{2\pi^2} J_B \left(\frac{M_{Z'}^2(\phi)}{T^2} \right), \quad (41)$$

where the bosonic thermal function is

$$J_B(x) = \int_0^\infty dz z^2 \log \left[1 - \exp\left(-\sqrt{z^2 + x}\right) \right]. \quad (42)$$

To improve the perturbative analysis beyond leading-order, we include in Eq. (40) the corrections due to the resummation of daisy diagrams [179]:

$$V_{\text{daisy}}(\phi, T) = \frac{T}{12\pi} \left[M_{Z'}^3(\phi) - M_{Z'}^3(\phi, T) \right], \quad (43)$$

where the field- and temperature-dependent gauge boson masses are given by⁶

$$M_{Z'}(\phi) = 2g'\phi, \quad M_{Z'}(\phi, T) = \sqrt{M_Z^2(\phi) + \Pi_{Z'}^2(T)}, \quad (44)$$

where $\Pi_{Z'}(T) = 2g'T$ is the thermal mass of the longitudinal component of the Z' boson.

⁶ Here, we have neglected the contribution from the λ -term to the thermal loop, since it is much smaller than the one from gauge interaction.

B. Strong first-order phase transition

To study the cosmological evolution of the effective potential (40), it is useful to approximate it as [159]

$$V_{\text{eff}}(\phi, u) \simeq \frac{1}{4}\lambda_{\text{eff}}(u)\phi^4 + \frac{1}{2}g'^2(u)T^2\phi^2, \quad (45)$$

with $\lambda_{\text{eff}} = 4\pi\alpha_\lambda(u)/(1 - \frac{b}{2\pi}\alpha_{g'}(0)u)^{a_2/b}$ [cf. Eq. (39)]. For $T \gg v_\Phi$, the effective potential has a unique minimum at $\phi = 0$. For $T \ll v_\Phi$, the self-coupling λ_{eff} around $\phi \lesssim T$ becomes negative, and therefore, $\phi = 0$ becomes a false vacuum. This takes place at the critical temperature $T_c \approx (2/3)g'v_\Phi$. We show the evolution of the effective potential at a few representative temperatures versus the field strength normalized by v_Φ in Fig. 16 (where for illustration, we take $M_{Z'} = 765$ GeV, which gives $T_c = 263$ GeV). For temperatures $T > T_c$, the true minimum is at $V_{\text{eff}} = 0$, as shown by the dot-dashed curve. At $T = T_c$ (dashed curve), the two minima are degenerate. As the temperature of the Universe drops below T_c , the minimum at $\phi = 0$ becomes the false vacuum ϕ_{false} (solid curve). At the nucleation temperature T_n (to be defined below), the field ϕ which is trapped around the false vacuum will tunnel to the true minimum, ϕ_{true} [180]. This transition is first-order, provided the transition rate exceeds the expansion rate of the Universe. In this case, the transition triggers bubble nucleation, and subsequent GW production.

The nucleation rate per unit volume is given by [181, 182]

$$\Gamma(T) = [A(T)]^4 \exp[-S(T)], \quad (46)$$

where A is a pre-factor of mass dimension one (see below), and S is the Euclidean bounce action. At zero temperature, the configuration minimizing the action is $O(4)$ -symmetric, and $S \equiv S_4$, where

$$S_4 = 2\pi^2 \int_0^\infty dr r^3 \left[\frac{1}{2} \left(\frac{d\phi}{dr} \right)^2 + V_{\text{eff}}(\phi, 0) \right], \quad (47)$$

and can be estimated using the saddle-point approximation from the equation of motion:

$$\frac{d^2\phi}{dr^2} + \frac{3}{r} \frac{d\phi}{dr} - \frac{\partial V_{\text{eff}}}{\partial\phi} = 0, \quad (48)$$

with the boundary conditions

$$\frac{d\phi}{dr}(r=0) = 0, \quad \phi(r=\infty) = 0. \quad (49)$$

In the above equation, the first condition is for the solution to be regular at the center of the bubble, and the second one is to describe the initial false vacuum background far from the bubble. The bubble nucleation rate is eventually well approximated at low T by $\Gamma \equiv \Gamma_4$, where [cf. Eq. (46)]

$$\Gamma_4 \simeq \frac{1}{R_c^4} \left(\frac{S_4}{2\pi} \right)^2 \exp(-S_4), \quad (50)$$

with $R_c \sim 1/T$ being the bubble radius in the low T limit.

At finite temperature, the field becomes periodic in the time coordinate (or in $1/T$). The configuration minimizing the action in this case is $O(3)$ -symmetric. Moreover, at sufficiently high temperatures, the minimum action configuration becomes constant in the time direction and $S \equiv S_3(T)/T$, where

$$S_3(T) = 4\pi \int_0^\infty dr r^2 \left[\frac{1}{2} \left(\frac{d\phi}{dr} \right)^2 + \Delta V_{\text{eff}}(\phi, T) \right], \quad (51)$$

where $\Delta V_{\text{eff}}(\phi, T) \equiv V_{\text{eff}}(\phi, T) - V_{\text{eff}}(\phi_{\text{false}}, T)$. Eq. (51) represents bubble formation through classical

field excitation over the barrier, with the corresponding equation of motion given by

$$\frac{d^2\phi}{dr^2} + \frac{2}{r} \frac{d\phi}{dr} - \frac{\partial V_{\text{eff}}}{\partial\phi} = 0, \quad (52)$$

with the same boundary conditions as in Eq. (49). The solution to Eq. (52) extremizes the action (51) that gives the exponential suppression of the false vacuum decay rate [183]. From Eq. (46), the nucleation rate $\Gamma \equiv \Gamma_3$ can be calculated as

$$\Gamma_3 \simeq T^4 \left(\frac{S_3(T)}{2\pi T} \right)^{3/2} \exp \left[-\frac{S_3(T)}{T} \right]. \quad (53)$$

In practice, the exact solution with a non-trivial periodic bounce in the time coordinate, which corresponds to quantum tunneling at finite temperature, is difficult to evaluate. Following Ref. [184], we have taken the minimum of the two actions S_3 and S_4 in our numerical calculation of the bubble nucleation rate, *i.e.*, $\Gamma \approx \max(\Gamma_3, \Gamma_4)$. For a discussion of related theoretical uncertainties, see Ref. [185].

The nucleation temperature is defined as the inverse time of creation of one bubble per Hubble radius, *i.e.*,

$$\frac{\Gamma(T)}{H(T)^4} \Big|_{T=T_n} = 1, \quad (54)$$

where the Hubble expansion rate at temperature T is $H(T) \simeq 1.66\sqrt{g_*}T^2/M_{\text{Pl}}$, with $g_* \simeq 110$ being the relativistic degrees of freedom at high temperatures,⁷ and $M_{\text{Pl}} \simeq 2.4 \times 10^{18}$ GeV being the reduced Planck mass.

The statistical analysis of the subsequent evolution of bubbles in the early Universe is crucial for SFOPT [187]. The probability for a given point to remain in the false vacuum is given by $P(T) = \exp[-I(T)]$ [188–191], where $I(T)$ is the expected volume of true vacuum bubbles per comoving volume:

$$I(T) = \frac{4\pi}{3} \int_T^{T_c} \frac{dT'}{T'^4} \frac{\Gamma(T')}{H(T')} \left(\int_T^{T'} \frac{d\tilde{T}}{H(\tilde{T})} \right)^3. \quad (55)$$

The change in the physical volume of the false vacuum, $\mathcal{V}_{\text{false}} = a^3(t)P(T)$ (with $a(t)$ being the scale factor and t being the time), normalized to the Hubble rate, is given by [192]

$$\frac{1}{\mathcal{V}_{\text{false}}} \frac{d\mathcal{V}_{\text{false}}}{dt} = H(T) \left(3 + T \frac{dI(T)}{dT} \right). \quad (56)$$

We define the percolation temperature T_p as satisfying the condition $I(T_p) = 0.34$ [187], while ensuring that the volume of the false vacuum is decreasing, *i.e.*, $d \log \mathcal{V}_{\text{false}}/dt < 0$, so that percolation is possible despite the exponential expansion of the false vacuum. Numerically, we find that the percolation temperature is only slightly smaller than the nucleation temperature, which in turn is smaller than the critical temperature. Moreover, as expected, both T_c and $T_n \simeq T_p$ grow monotonically, as either of the model parameters, $M_{Z'}$ or g' , increases. They are depicted in Fig. 17.

The strength of the phase transition is characterized by two quantities α and β defined as follows: $\alpha = \epsilon_*/\rho_{\text{rad}}$ is the ratio of the vacuum energy density ϵ_* released in the transition to the radiation energy density $\rho_{\text{rad}} = \pi^2 g_* T_*^4/30$, both evaluated at $T = T_*$ (where T_* is either T_n or T_p).⁸ The vacuum energy density is nothing but the free energy difference between the true and false vacua [193], thus yielding

$$\alpha = \frac{1}{\rho_{\text{rad}}} \left(-1 + T \frac{d}{dT} \right) \Delta V_{\text{min}} \Big|_{T=T_*}, \quad (57)$$

⁷ In our numerical analysis, we take into account the temperature-dependence of g_* [186].

⁸ Calculating α at T_p is better, as it accounts for the entropy dilution between T_n and T_p , although this distinction becomes irrelevant for the GW signal when $\alpha \gg 1$.

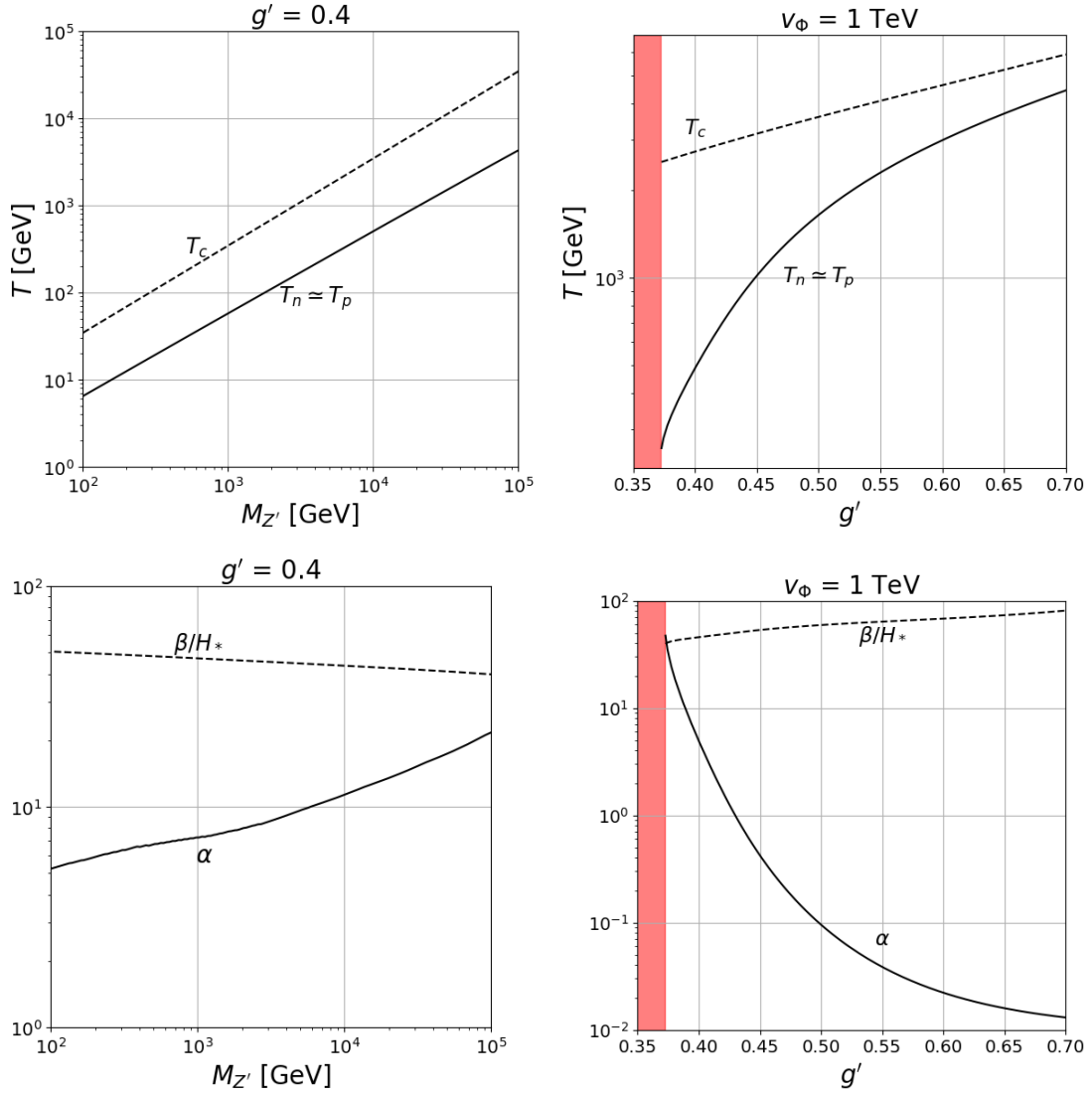


FIG. 17. Variation of the temperatures T_c , T_n and T_p (upper panels) and the phase transition parameters α and β/H_* (lower panels) with respect to the model parameters $M_{Z'}$ (left) and g' (right), keeping the other ones fixed at the values shown in the plots. The red region on the right panels corresponds to the lower limit on the gauge coupling below which the rate of phase transition is not fast enough with respect to the Hubble rate H to achieve bubble nucleation.

where ΔV_{\min} is the temperature-dependent minimum of the effective potential ΔV_{eff} defined below Eq. (51).

The second important parameter is β/H_* , where β is the (approximate) inverse timescale of the phase transition and H_* is the Hubble rate at T_* :

$$\frac{\beta}{H_*} = -\frac{T}{\Gamma} \frac{d\Gamma}{dT} \Big|_{T=T_*}. \quad (58)$$

For strong transitions, β is related to the average bubble radius R_* : $\beta = (8\pi)^{1/3}/R_*$ [164],⁹ where R_* defines the characteristic length scale of transition and is given by [191, 192]

$$R_* = \left[T_* \int_{T_*}^{T_c} \frac{dT}{T^2} \frac{\Gamma(T)}{H(T)} \exp\{-I(T)\} \right]^{-1/3}. \quad (59)$$

⁹ When identifying β/H_* with the average bubble radius, it is numerically found that taking $T_* = T_n$ gives a more accurate result [194].

The variation of α and β/H_* with the model parameters g' and $M_{Z'}$ is shown in Fig. 17. We find that β/H_* decreases (increases) with increasing $M_{Z'}$ (g'), whereas α has the opposite behavior. Moreover, the change in α is more rapid than that in β/H_* . We also find that the gauge coupling cannot be decreased arbitrarily, because below a certain value (as shown by the red shaded region on the right panels of Fig. 17), the rate of transition is not fast enough with respect to the Hubble rate H to achieve bubble nucleation.

C. Gravitational wave spectrum

The amplitude of the GW signal as a function of the frequency f is usually defined as

$$h^2\Omega_{\text{GW}}(f) \equiv \frac{h^2}{\rho_c} \frac{d\rho_{\text{GW}}}{d\log f}, \quad (60)$$

where $h \sim 0.7$ is the dimensionless Hubble parameter (defined in terms of today's value of H , $H_0 = 100h$ km/s/Mpc), ρ_{GW} is the energy density released in the form of GWs, and $\rho_c = 3H_0^2 M_{\text{Pl}}^2 \simeq 1.05 \times 10^{-5} h^2$ GeV/cm³ is the critical density of the Universe. The reason for multiplying Ω_{GW} by h^2 is to make sure that the GW amplitude is not affected by the experimental uncertainty [195] in the Hubble parameter H_0 .

There are three different mechanisms for producing GWs in an SFOPT from the expanding and colliding scalar-field bubbles, as well as from their interaction with the thermal plasma. These are: (i) collisions of expanding bubble walls [196–206], compressional modes (or sound waves) in the bulk plasma [207–213], and (iii) vortical motion (or magnetohydrodynamic turbulence) in the bulk plasma [214–220]. The total GW signal can be approximated as a linear superposition of the signals generated from these three individual sources, denoted respectively by Ω_b (bubble wall), Ω_s (sound wave), and Ω_t (turbulence):

$$h^2\Omega_{\text{GW}}(f) \simeq h^2\Omega_b(f) + h^2\Omega_s(f) + h^2\Omega_t(f). \quad (61)$$

The three contributions can be parameterized in a model-independent way in terms of a set of characteristic SFOPT parameters, namely, α [cf. Eq. (57)], β/H_* [cf. Eq. (58)], T_* ,¹⁰ bubble-wall velocity v_w , and the three efficiency factors κ_b , κ_s , κ_t that characterize the fractions of the released vacuum energy that are converted into the energy of scalar field gradients, sound waves and turbulence, respectively. The bubble-wall velocity in the plasma rest-frame is given by [222]

$$v_w = \begin{cases} \sqrt{\frac{\Delta V_{\text{min}}}{\alpha\rho_{\text{rad}}}} & \text{for } \frac{\Delta V_{\text{min}}}{\alpha\rho_{\text{rad}}} < v_J \\ 1 & \text{for } \frac{\Delta V_{\text{min}}}{\alpha\rho_{\text{rad}}} \geq v_J \end{cases}, \quad (62)$$

where $v_J = (1 + \sqrt{3\alpha^2 + 2\alpha})/\sqrt{3}(1 + \alpha)$ is the Jouguet velocity [199, 223, 224]. As for the efficiency factors, it is customary to express κ_s and κ_t in terms of another efficiency factor κ_{kin} that characterizes the energy fraction converted into bulk kinetic energy and an additional parameter ε , *i.e.* [225]

$$\kappa_s = \kappa_{\text{kin}}, \quad \kappa_t = \varepsilon\kappa_{\text{kin}}. \quad (63)$$

While the precise numerical value of ε is still under debate, following Refs. [210, 226], we will use $\varepsilon = 1$. The efficiency factor κ_b is taken from Ref. [199] and κ_{kin} is taken from Ref. [224], both of

¹⁰ We will use $T_* = T_n$, the nucleation temperature defined in Eq. (54). For subtleties, see Ref. [221].

which were calculated in the so-called Jouguet detonation limit:

$$\begin{aligned}\kappa_b &= \frac{1}{(1 + 0.715\alpha)} \left(0.715\alpha + \frac{4}{27} \sqrt{\frac{3\alpha}{2}} \right), \\ \kappa_{\text{kin}} &= \frac{\sqrt{\alpha}}{(0.135 + \sqrt{0.98 + \alpha})}.\end{aligned}\tag{64}$$

Each of the three contributions in Eq. (61) is related to the SFOPT parameters discussed above, as follows [227]:

$$h^2\Omega_i(f) = h^2\Omega_i^{\text{peak}} \left(\alpha, \frac{\beta}{H_*}, T_*, v_w, \kappa_i \right) \mathcal{S}_i(f, f_i),\tag{65}$$

where $i \in \{b, s, t\}$, the peak amplitudes are given as [226]

$$\begin{aligned}h^2\Omega_b^{\text{peak}} &\simeq 1.67 \times 10^{-5} \left(\frac{v_w}{\beta/H_*} \right)^2 \left(\frac{100}{g_*(T_*)} \right)^{1/3} \left(\frac{\kappa_b\alpha}{1 + \alpha} \right)^2 \left(\frac{0.11v_w}{0.42 + v_w^2} \right), \\ h^2\Omega_s^{\text{peak}} &\simeq 2.65 \times 10^{-6} \left(\frac{v_w}{\beta/H_*} \right) \left(\frac{100}{g_*(T_*)} \right)^{1/3} \left(\frac{\kappa_s\alpha}{1 + \alpha} \right)^2, \\ h^2\Omega_t^{\text{peak}} &\simeq 3.35 \times 10^{-4} \left(\frac{v_w}{\beta/H_*} \right) \left(\frac{100}{g_*(T_*)} \right)^{1/3} \left(\frac{\kappa_t\alpha}{1 + \alpha} \right)^{3/2},\end{aligned}\tag{66}$$

and the spectral shape functions are given as [226]

$$\begin{aligned}\mathcal{S}_b(f, f_b) &= \left(\frac{f}{f_b} \right)^{2.8} \left[\frac{3.8}{1 + 2.8(f/f_b)^{3.8}} \right], \\ \mathcal{S}_s(f, f_s) &= \left(\frac{f}{f_s} \right)^3 \left[\frac{7}{4 + 3(f/f_s)^2} \right]^{7/2}, \\ \mathcal{S}_t(f, f_t, h_*) &= \left(\frac{f}{f_t} \right)^3 \left[\frac{1}{1 + (f/f_t)} \right]^{11/3} \left(\frac{1}{1 + 8\pi f/h_*} \right).\end{aligned}\tag{67}$$

Note that \mathcal{S}_b and \mathcal{S}_s are normalized to unity at their respective peak frequencies f_b and f_s , whereas \mathcal{S}_t at f_t depends on the Hubble frequency

$$h_* = \frac{a_*}{a_0} H_* = 1.6 \times 10^{-2} \text{ mHz} \left(\frac{g_*(T_*)}{100} \right)^{1/6} \left(\frac{T_*}{100 \text{ GeV}} \right).\tag{68}$$

And finally, the peak frequencies are given as

$$\begin{aligned}f_b &= 1.6 \times 10^{-2} \text{ mHz} \left(\frac{g_*(T_*)}{100} \right)^{1/6} \left(\frac{T_*}{100 \text{ GeV}} \right) \left(\frac{\beta/H_*}{v_w} \right) \left(\frac{0.62v_w}{1.8 - 0.1v_w + v_w^2} \right), \\ f_s &= 1.9 \times 10^{-2} \text{ mHz} \left(\frac{g_*(T_*)}{100} \right)^{1/6} \left(\frac{T_*}{100 \text{ GeV}} \right) \left(\frac{\beta/H_*}{v_w} \right), \\ f_t &= 2.7 \times 10^{-2} \text{ mHz} \left(\frac{g_*(T_*)}{100} \right)^{1/6} \left(\frac{T_*}{100 \text{ GeV}} \right) \left(\frac{\beta/H_*}{v_w} \right).\end{aligned}\tag{69}$$

Since there are only two free parameters in our model setup, namely, $M_{Z'}$ (or v_Φ) and g' , we show in Fig. 18 how the total GW amplitude as a function of the GW frequency varies with respect to these two model parameters. In the left panel, we fix $g' = 0.4$ and show the GW spectra for different values of $M_{Z'}$ (or equivalently, the VEV v_Φ). It is clear that the whole spectrum shifts to higher frequencies with increasing $M_{Z'}$, which is due to the correlation of the symmetry-breaking scale

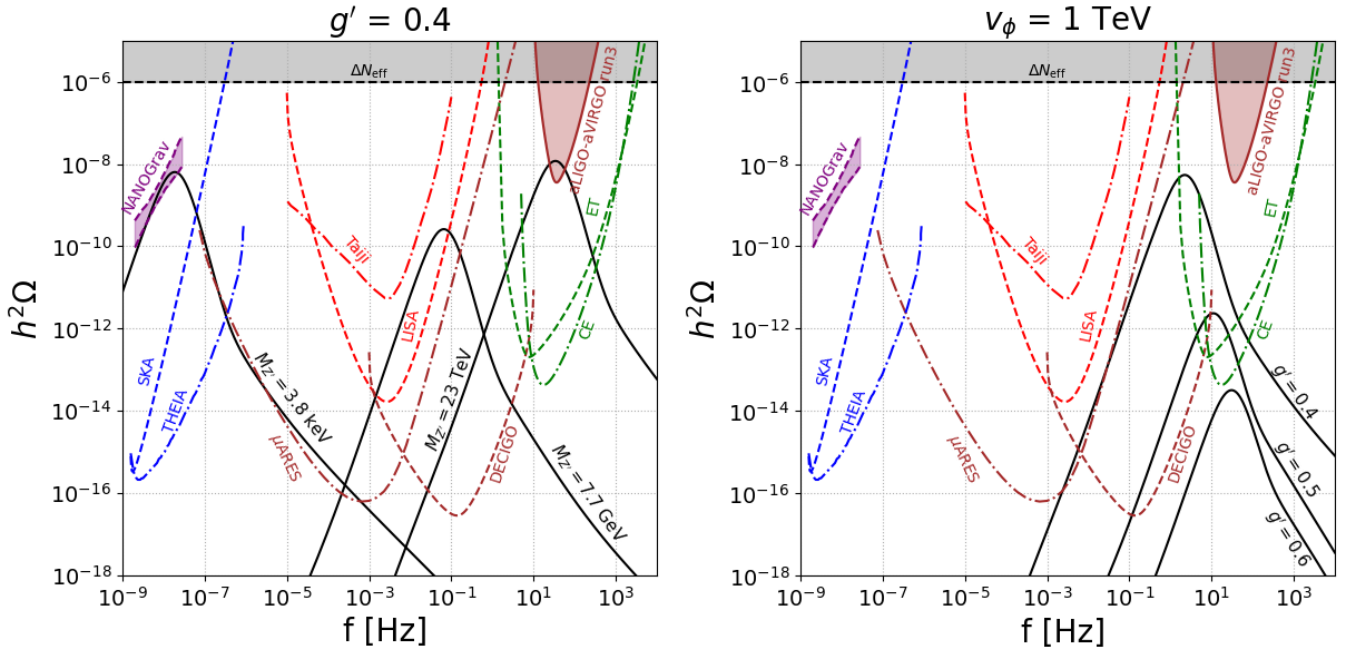


FIG. 18. The stochastic GW amplitude in the $U(1)_{L_\alpha-L_\beta}$ models for different values of the Z' mass $M_{Z'}$ (left panel) and gauge coupling g' (right panel), while keeping the other parameter fixed at the value shown in the plot. The current constraints from aLIGO-aVIRGO, ΔN_{eff} , as well as the future sensitivities from planned GW experiments are shown for comparison. The recent NANOGrav observations in the nHz regime are also shown.

with the nucleation temperature, which in turn moves the peak frequency [cf. Eq. (69)]. The peak amplitude increases with $M_{Z'}$, which is mostly due to its correlation with α , and to a lesser extent, with β/H_* [cf. Eq. (66) and Fig. 17]. For very small $M_{Z'}$ values, the peak amplitude again starts to increase because of the smaller g_* . For comparison, we also show the current 95% CL constraint on the stochastic GW amplitude from aLIGO-aVIRGO third run [37] (red shaded region on the upper right corner), as well as the 95% CL constraint on $\Delta N_{\text{eff}} < 0.18$ from a joint BBN+CMB analysis [228], which translates into an upper bound on $h^2\Omega_{\text{GW}} \leq 5.6 \times 10^{-6} \Delta N_{\text{eff}}$ [229] (gray shaded region). The recent NANOGrav observation [44] is also shown in the upper left corner, which can in principle be fitted in our model for a keV-scale $M_{Z'}$ with $g' \simeq 0.4$; this parameter space is however excluded by low-energy laboratory constraints [86, 87]. There is a whole suite of proposed GW experiments at various frequencies (from nHz to kHz), such as SKA [230], GAIA/THEIA [231], MAGIS [232], AION [233], AEDGE [234], μARES [38], LISA [39], TianQin [235], Taiji [236], DECIGO [40], BBO [41], ET [42], CE [43], as well as recent proposals for high-frequency GW searches in the MHz-GHz regime [237–240]. The projected sensitivities of a selected subset of these planned experiments are shown in Fig. 18 by the dashed/dot-dashed curves. The experiments above the mHz frequency are the most relevant ones for us, since they will probe the region around or above electroweak-scale $M_{Z'}$, complementary to the collider searches (see Section IV D).

In the right panel of Fig. 18, we show the GW spectra with $v_\Phi = 1$ TeV for different values of g' . As g' increases, α decreases and β/H_* increases (cf. Fig. 17). Therefore, the peak amplitude goes down, while the peak frequency slightly shifts to higher values due to the slow increase in β/H_* . This gives an upper bound on g' for a given $M_{Z'}$ when we require that the GW amplitude is within the sensitivity range of a given experiment. On the other hand, as g' decreases, (Γ/H^4) at T_* eventually becomes smaller than one, which no longer allows bubble nucleation. This, in turn, gives a lower limit on g' for a given $M_{Z'}$ [cf. the red shaded region in Fig. 17 right panels] so that the first-order phase transition can happen. We will exploit this feature in Section IV D to show the model parameter space accessible at future GW experiments.

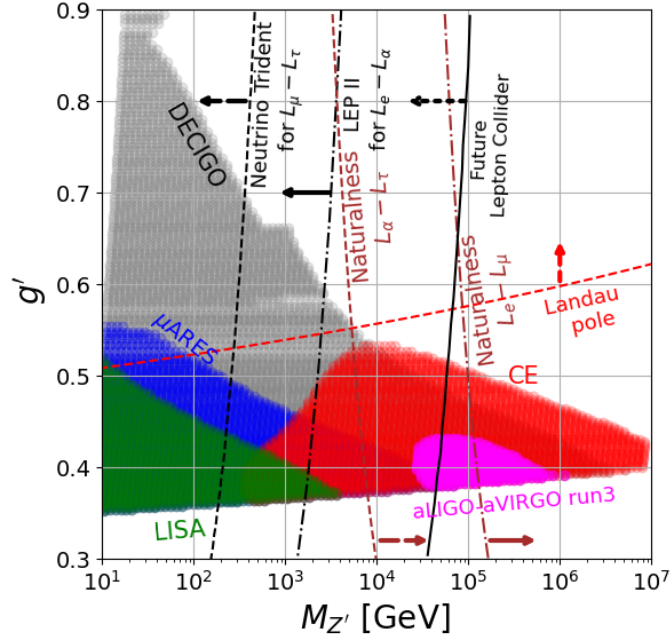


FIG. 19. Discovery sensitivity (with $\text{SNR} > 10$) of the future GW experiments μARES , LISA, DECIGO and CE in the $(M_{Z'}, g')$ plane. The current constraint from aLIGO-aVIRGO run 3 (with $\text{SNR} > 0.1$) is also shown. The most stringent laboratory constraints from LEP-2 and neutrino trident experiments are shown for comparison (with the arrow pointing to the exclusion region), along with the future collider sensitivity (dot-dashed line). The naturalness and perturbativity (Landau pole) constraints are also shown; see Section IV E.

D. Complementarity with other laboratory constraints

To estimate the stochastic GW signal strength for the ongoing GW experiments and also to obtain predictions for the future ones, we calculate the signal-to-noise ratio (SNR) ρ for a given experiment by using its noise curve and by integrating over the observing time t_{obs} and accessible frequency range $[f_{\text{min}}, f_{\text{max}}]$ [241–245]:

$$\rho = \left[n_{\text{det}} t_{\text{obs}} \int_{f_{\text{min}}}^{f_{\text{max}}} df \left(\frac{\Omega_{\text{GW}}(f) h^2}{\Omega_{\text{noise}}(f) h^2} \right)^2 \right]^{1/2}. \quad (70)$$

Here n_{det} distinguishes between experiments aiming at detecting the GW by means of an auto-correlation ($n_{\text{det}} = 1$) or a cross-correlation ($n_{\text{det}} = 2$) measurement. For our numerical analysis, we assume $n_{\text{det}} = 1$ and take an observation period of $t_{\text{obs}} = 1$ year for each experiment. To register a detection, we demand $\rho > \rho_{\text{th}}$ for some chosen threshold SNR value ρ_{th} . With this standard, we present the potential discovery sensitivity with $\rho_{\text{th}} = 10$ in the plane of $(M_{Z'}, g')$ in Fig. 19 for three proposed experiments, namely, μARES [38] (blue), LISA [39] (green), DECIGO [40] (grey) and CE [43] (red), which are chosen for illustration in order to cover a wide frequency range, and hence, a wide range of $M_{Z'}$.

These sensitivities are equally applicable for any flavor combination of the $U(1)_{L_\alpha - L_\beta}$ models. For comparison, we also show the most stringent laboratory constraint, which comes from LEP-2 for $U(1)_{L_e - L_\alpha}$, and from neutrino trident for $U(1)_{L_\mu - L_\tau}$ [cf. Fig. 2], as shown by the dashed/solid lines with the arrow pointing to the exclusion region. The best sensitivity at high Z' masses coming from the Bhabha channel at e^+e^- and $\mu^+\mu^-$ colliders [cf. Fig. 15] is shown by the dot-dashed line. We see that future GW experiments have great potential for discovery and the theory parameter coverage corresponds up to $M_{Z'} \approx 4,000$ TeV. It extends the energy scale probe far beyond the collider regime, as long as the gauge coupling is sizable to produce an observable GW signal. In fact,

using the existing upper limit on the GW amplitude from the third run of aLIGO-aVIRGO, we can already exclude a tiny part of the high- $M_{Z'}$ parameter space between 20 – 200 TeV, as shown by the magenta region in Fig. 19. However, this is currently possible only for a lower SNR threshold of $\rho_{\text{th}} = 0.1$.

Additional correlations between the GW signal and the collider signals could stem from the scalar sector of the model, depending on the strength of the quartic coupling $\lambda'(H^\dagger H)(\Phi^\dagger \Phi)$ in the scalar potential (32). This term induces a mixing between the SM Higgs and the extra physical scalar ϕ . This mixing in turn induces modifications in precision electroweak observables, as well as in the SM Higgs signal strengths [246, 247]. The current LHC constraints imply that the mixing angle $\sin \theta \lesssim 0.15$ for a TeV-scale scalar [248], and this can be significantly improved at a future lepton collider [249, 250]. One can also directly search for the new scalar by its decay into SM fermions, gauge bosons or Higgs pairs. For a summary of the current constraints and future prospects in the scalar mass-mixing plane, see e.g. Refs. [251, 252]. In addition, in the $U(1)$ models considered here, the scalar can decay into a pair of Z' bosons or into a pair of right-handed neutrino (in extended models) [253], if kinematically allowed. Similarly, if the scalar and Z' are light enough, they can be pair-produced from the SM Higgs decay [254].

E. Theoretical constraints

As the original theory adheres to classical conformal principles and is established as a massless theory, the self-energy corrections to the SM Higgs boson stem from modifications to the mixing quartic coupling λ' in Eq. (32). This can be computed within the effective Higgs potential as follows:

$$V_{\text{eff}} \supset \frac{\lambda'}{4} \phi^2 h^2 + \frac{\beta_{\text{mix}}}{8} \phi^2 h^2 (\log [\phi^2] + C), \quad (71)$$

where the logarithmic divergence and terms not dependent on ϕ are all encapsulated in C . In the $U(1)_{L_\alpha - L_\beta}$ model we have, the principal contribution to the β -function comes from the two-loop diagrams involving the Z' boson and leptons [32, 255]:

$$\beta_{\text{mix}} \supset -\frac{9g^4 m_\ell^2}{8\pi^4 v^2}, \quad \text{where } m_\ell = \max\{m_{\ell_\alpha}, m_{\ell_\beta}\}. \quad (72)$$

By adding a counterterm, we renormalize the coupling λ' with the renormalization condition:

$$\left. \frac{\partial^2 V_{\text{eff}}}{\partial h^2 \partial \phi^2} \right|_{h=0, \phi=v_\phi} = \lambda', \quad (73)$$

where λ' is the renormalized coupling. This results in the following potential:

$$V_{\text{eff}} \supset \frac{\lambda'}{4} \phi^2 h^2 + \frac{\beta_{\text{mix}}}{8} \phi^2 h^2 \left(\ln \left[\frac{\phi^2}{v_\Phi^2} \right] - 3 \right). \quad (74)$$

Substituting $\phi = v_\Phi$, we obtain the SM Higgs mass correction as

$$\delta m_h^2 = -\frac{3}{4} \beta_{\text{mix}} v_\Phi^2 \simeq \frac{27g^4 m_\ell^2 v_\Phi^2}{32\pi^4 v^2}. \quad (75)$$

If δm_h^2 is much larger than the electroweak scale, we need a fine-tuning of the tree-level Higgs mass $m_h^2 = \lambda' v_\Phi^2$ to reproduce the correct electroweak VEV. Therefore, we can introduce a fine-tuning measure as $r \equiv m_h^2 / \delta m_h^2$. For instance, $r = 0.1$ indicates that we need to fine-tune the tree-level Higgs mass squared at the 10% accuracy level. This is indicated in Fig. 19 by the solid and dashed red curves for $U(1)_{L_e - L_\mu}$ and $U(1)_{L_\alpha - L_\tau}$, respectively. The region to the right of these curves are disfavored by naturalness. However, it is worth emphasizing that these naturalness constraints are

subjective ($r = 0.1$ is just an arbitrary choice), and should not be treated at the same level as the *experimental* constraints. Nonetheless, we find from Fig. 19 that the future colliders should be able to probe a large fraction of the Z' parameter space allowed by naturalness and Landau pole constraints.

Another theoretical constraint that typically appears for large couplings is the perturbativity constraint. The requirement that the gauge coupling remains perturbative and does not blow up all the way up to the Planck scale is shown by the red dashed curve in Fig. 19, where the region above it is disfavored. This is obtained from the RG running of the gauge coupling in our model, cf. Eq. (36). We note that this constraint can be relaxed if there is some new physics between the Z' scale and the Planck scale that might alter the RG evolution.

V. SUMMARY AND CONCLUSIONS

In this article, we studied the phenomenology of leptophilic Z' gauge bosons around the electroweak-scale mass range in the anomaly-free $U(1)_{L_\alpha-L_\beta}$ models at the future high energy e^+e^- and $\mu^+\mu^-$ colliders, as well as at gravitational wave observatories. The two independent parameters of the model are the mass of the Z' boson ($M_{Z'}$) and its coupling to the leptons (g'). We first summarized the existing bounds on the model parameters from low energy to collider searches in Section II B. As depicted in Fig. 2, a large parameter space with $M_{Z'} \gtrsim 100$ GeV and g' up to $\mathcal{O}(0.1)$ is still unexplored.

In Section III, we analyzed in great detail the Z' phenomenology at future lepton colliders. We considered a representative collider center-of-mass energy of 3 TeV [7, 10]. For the considered parameter space, the Z' decays promptly. We considered various production channels such as resonant production of Z' via the radiative return, production in association with an observable photon, and the scenario where Z' is produced via the radiation of the final-state lepton. As shown in the plots of Fig. 4 and Fig. 5, the resonant production of Z' is characterized by a resonance peak at $\sqrt{s} \simeq M_{Z'}$. For $\sqrt{s} > M_{Z'}$ the ISR effect facilitates the on-shell Z' production. The SM processes that mimic the signal are dilepton production via s - or t -channel exchange of the photon and Z boson, as well as a 4-lepton final state via electroweak VBF, where two forward-backward leptons remain undetected. The VBF processes have a sizable contribution to the SM background, particularly in the off-resonance region. The signal shows distinct kinematic features in the invariant dilepton mass $M_{\ell\ell}$, the rapidity $y_{\ell\ell}$, and the cosine angle of the final state leptons, which are used to discriminate the Z' signal from the SM background. We presented the 2σ sensitivity limit in $(M_{Z'}, g')$ plane as shown in Fig. 15. We find that couplings down to $g' \sim 10^{-3}$ can be probed for $M_{Z'} \lesssim \sqrt{s}$, whereas in the off-shell regime $M_{Z'} > \sqrt{s}$, the sensitivity varies between $g' \simeq 0.01 - 0.1$ for $M_{Z'} \simeq 3 - 10$ TeV.

In Section III C, we analyzed a complementary production mechanism of the Z' in association with an observable photon, *i.e.*, $e^+e^-, \mu^+\mu^- \rightarrow Z'\gamma \rightarrow \ell^+\ell^-\gamma$ by demanding photon acceptance cuts Eq. (26). Similar to the Z' production via ISR, it exhibits resonance peak and enhancement in signal rate for $\sqrt{s} > M_{Z'}$. It is important to note that, because of the identification of a final state photon, one can use the recoil mass M_{recoil} of the photon to reconstruct the Z' mass peak, regardless the decay, including the invisible mode to a neutrino pair, leading to the spectacular mono-photon plus missing energy final state. However, the signal rate for this case is smaller due to the radiation of an extra hard photon. The annihilation processes mediated via γ/Z are the primary background, and the VBF processes are very much suppressed in this case, as shown in Fig. 9 and Fig. 10. With the similar invariant mass cut, we select the signal events and calculate the 2σ sensitivity limit. As the VBF background is suppressed, we do not use rapidity cut though there is a wide peak at $|y_{Z'}|$. The 2σ sensitivity limit is shown by the magenta lines in Fig. 15. This channel provides the best sensitivity for the $L_e - L_\mu$ model in the mass range 100 to 300 GeV, whereas, for the $L_e - L_\tau$ and $L_\mu - L_\tau$ models, the lower reconstruction efficiency of final state τ slightly reduces the sensitivity.

We have also considered the scenarios in which the Z' does not couple to the beam leptons, and therefore, cannot be produced via direct annihilation. Instead, the Z' boson can be produced as radiation off the final state leptons. Subsequent decay of Z' to lepton pair leads to a four-lepton final state that serves as the signal for this scenario. Using the invariant mass cut as defined in Eq. (17),

we presented 2σ limit shown by red and orange curves in Fig. 15. Although this channel shows lower sensitivity due to a lower signal rate and a relatively larger background, it is still promising for the search in such a challenging model.

We further studied the cosmological implications of this model at the early universe in Section IV. Interestingly, if these $U(1)$ models are classically conformally invariant, the phase transition at the $U(1)$ symmetry-breaking scale tends to be strongly first-order with ultra-supercooling, leading to observable stochastic gravitational wave signatures. We calculated the GW signals in a conformal version of the $U(1)_{L_\alpha-L_\beta}$ models under discussion, which are complementary to our collider signals. We observed in Fig. 19 that the GW signal generated via SFOPT occurs for relatively large gauge coupling $g' \in [0.35, 0.55]$. Depending on the frequency range of the GW detectors, we can probe $M_{Z'}$ up to several thousand TeV, well beyond the reach of colliders. In fact, the recent null results from advanced LIGO-VIRGO run 3 on the stochastic GW searches have already ruled out a small portion of the high-mass range $M_{Z'} \in [20 \text{ TeV}, 1 \text{ PeV}]$ and gauge coupling ranging from $g' \in [0.37, 0.44]$. We concluded that more parameter space will be susceptible to future GW observatories like LISA, μ ARES and Cosmic Explorer.

In summary, we showed the complementarity between future colliders and the GW experiments in probing the Z' parameter space preferred by naturalness and Landau pole constraints.

ACKNOWLEDGMENTS

This work was supported in part by the U.S. Department of Energy under grant Nos. DE-SC0007914 and in part by the Pitt PACC. The work of BD, TH, and KX was performed partly at the Aspen Center for Physics, which is supported by the National Science Foundation under grant No. PHY-1607611 and No. PHY-2210452. The work of KX was also supported by the National Science Foundation under grant No. PHY-2112829, No. PHY-2013791, and No. PHY-2310497. This work used resources of high-performance computing clusters from the Pitt CRC. The work of BD is supported in part by the U.S. Department of Energy under grant No. DE-SC0017987 and by a URA VSP Fellowship. RP acknowledges financial support for this research by the Fulbright U.S. Student Program, which is sponsored by the U.S. Department of State and The United States – India Educational Foundation (USIEF).

-
- [1] **Particle Data Group** Collaboration, R. L. Workman *et al.*, “Review of Particle Physics,” [PTEP](#) **2022** (2022) 083C01.
 - [2] **LEP, ALEPH, DELPHI, L3, OPAL, LEP Electroweak Working Group, SLD Electroweak Group, SLD Heavy Flavor Group** Collaboration, t. S. Electroweak, “A Combination of preliminary electroweak measurements and constraints on the standard model,” [arXiv:hep-ex/0312023](#).
 - [3] **ALEPH, DELPHI, L3, OPAL, LEP Electroweak** Collaboration, S. Schael *et al.*, “Electroweak Measurements in Electron-Positron Collisions at W-Boson-Pair Energies at LEP,” [Phys. Rept.](#) **532** (2013) 119–244, [arXiv:1302.3415 \[hep-ex\]](#).
 - [4] **ILC** Collaboration, “The International Linear Collider Technical Design Report - Volume 2: Physics,” [arXiv:1306.6352 \[hep-ph\]](#).
 - [5] **CEPC Study Group** Collaboration, M. Dong *et al.*, “CEPC Conceptual Design Report: Volume 2 - Physics & Detector,” [arXiv:1811.10545 \[hep-ex\]](#).
 - [6] **FCC** Collaboration, A. Abada *et al.*, “FCC-ee: The Lepton Collider: Future Circular Collider Conceptual Design Report Volume 2,” [Eur. Phys. J. ST](#) **228** no. 2, (2019) 261–623.
 - [7] **CLICdp, CLIC** Collaboration, T. K. Charles *et al.*, “The Compact Linear Collider (CLIC) - 2018 Summary Report,” [arXiv:1812.06018 \[physics.acc-ph\]](#).
 - [8] J. P. Delahaye, M. Diemoz, K. Long, B. Mansoulié, N. Pastrone, L. Rivkin, D. Schulte, A. Skrinsky, and A. Wulzer, “Muon Colliders,” [arXiv:1901.06150 \[physics.acc-ph\]](#).

- [9] K. Long, D. Lucchesi, M. Palmer, N. Pastrone, D. Schulte, and V. Shiltsev, “Muon colliders to expand frontiers of particle physics,” *Nature Phys.* **17** no. 3, (2021) 289–292, [arXiv:2007.15684 \[physics.acc-ph\]](#).
- [10] **Muon Collider** Collaboration, J. de Blas *et al.*, “The physics case of a 3 TeV muon collider stage,” [arXiv:2203.07261 \[hep-ph\]](#).
- [11] C. Accettura *et al.*, “Towards a Muon Collider,” [arXiv:2303.08533 \[physics.acc-ph\]](#).
- [12] P. Langacker, “The Physics of Heavy Z' Gauge Bosons,” *Rev. Mod. Phys.* **81** (2009) 1199–1228, [arXiv:0801.1345 \[hep-ph\]](#).
- [13] R. Foot, “New Physics From Electric Charge Quantization?,” *Mod. Phys. Lett. A* **6** (1991) 527–530.
- [14] X.-G. He, G. C. Joshi, H. Lew, and R. R. Volkas, “Simplest Z-prime model,” *Phys. Rev. D* **44** (1991) 2118–2132.
- [15] R. Foot, X. G. He, H. Lew, and R. R. Volkas, “Model for a light Z-prime boson,” *Phys. Rev. D* **50** (1994) 4571–4580, [arXiv:hep-ph/9401250](#).
- [16] B. A. Dobrescu and F. Yu, “Dijet and electroweak limits on a Z' boson coupled to quarks,” [arXiv:2112.05392 \[hep-ph\]](#).
- [17] P. J. Fox and E. Poppitz, “Leptophilic Dark Matter,” *Phys. Rev. D* **79** (2009) 083528, [arXiv:0811.0399 \[hep-ph\]](#).
- [18] J. Kopp, V. Niro, T. Schwetz, and J. Zupan, “DAMA/LIBRA and leptonically interacting Dark Matter,” *Phys. Rev. D* **80** (2009) 083502, [arXiv:0907.3159 \[hep-ph\]](#).
- [19] P. Agrawal, Z. Chacko, and C. B. Verhaaren, “Leptophilic Dark Matter and the Anomalous Magnetic Moment of the Muon,” *JHEP* **08** (2014) 147, [arXiv:1402.7369 \[hep-ph\]](#).
- [20] N. F. Bell, Y. Cai, R. K. Leane, and A. D. Medina, “Leptophilic dark matter with Z' interactions,” *Phys. Rev. D* **90** no. 3, (2014) 035027, [arXiv:1407.3001 \[hep-ph\]](#).
- [21] A. Alves, A. Berlin, S. Profumo, and F. S. Queiroz, “Dark Matter Complementarity and the Z' Portal,” *Phys. Rev. D* **92** no. 8, (2015) 083004, [arXiv:1501.03490 \[hep-ph\]](#).
- [22] C. Blanco, M. Escudero, D. Hooper, and S. J. Witte, “ Z' mediated WIMPs: dead, dying, or soon to be detected?,” *JCAP* **11** (2019) 024, [arXiv:1907.05893 \[hep-ph\]](#).
- [23] K. A. Meissner and H. Nicolai, “Conformal Symmetry and the Standard Model,” *Phys. Lett. B* **648** (2007) 312–317, [arXiv:hep-th/0612165](#).
- [24] A. Farzinnia and J. Ren, “Strongly First-Order Electroweak Phase Transition and Classical Scale Invariance,” *Phys. Rev. D* **90** no. 7, (2014) 075012, [arXiv:1408.3533 \[hep-ph\]](#).
- [25] G. 't Hooft, “Naturalness, chiral symmetry, and spontaneous chiral symmetry breaking,” *NATO Sci. Ser. B* **59** (1980) 135–157.
- [26] E. Gildener, “Gauge Symmetry Hierarchies,” *Phys. Rev. D* **14** (1976) 1667.
- [27] S. Weinberg, “Gauge Hierarchies,” *Phys. Lett. B* **82** (1979) 387–391.
- [28] Y. Kawamura, “Naturalness, Conformal Symmetry and Duality,” *PTEP* **2013** no. 11, (2013) 113B04, [arXiv:1308.5069 \[hep-ph\]](#).
- [29] S. R. Coleman and E. J. Weinberg, “Radiative Corrections as the Origin of Spontaneous Symmetry Breaking,” *Phys. Rev. D* **7** (1973) 1888–1910.
- [30] K. Fujikawa, “Heavy Fermions in the Standard Sequential Scheme,” *Prog. Theor. Phys.* **61** (1979) 1186.
- [31] S. Iso, N. Okada, and Y. Orikasa, “Classically conformal B-L extended Standard Model,” *Phys. Lett. B* **676** (2009) 81–87, [arXiv:0902.4050 \[hep-ph\]](#).
- [32] S. Iso, N. Okada, and Y. Orikasa, “The minimal B-L model naturally realized at TeV scale,” *Phys. Rev. D* **80** (2009) 115007, [arXiv:0909.0128 \[hep-ph\]](#).
- [33] S. Iso and Y. Orikasa, “TeV Scale B-L model with a flat Higgs potential at the Planck scale: In view of the hierarchy problem,” *PTEP* **2013** (2013) 023B08, [arXiv:1210.2848 \[hep-ph\]](#).
- [34] S. Oda, N. Okada, and D.-s. Takahashi, “Classically conformal $U(1)'$ extended standard model and Higgs vacuum stability,” *Phys. Rev. D* **92** no. 1, (2015) 015026, [arXiv:1504.06291 \[hep-ph\]](#).
- [35] J. Guo, Z. Kang, P. Ko, and Y. Orikasa, “Accidental dark matter: Case in the scale invariant local B-L model,” *Phys. Rev. D* **91** no. 11, (2015) 115017, [arXiv:1502.00508 \[hep-ph\]](#).

- [36] A. Das, S. Oda, N. Okada, and D.-s. Takahashi, “Classically conformal $U(1)$ ’ extended standard model, electroweak vacuum stability, and LHC Run-2 bounds,” *Phys. Rev. D* **93** no. 11, (2016) 115038, [arXiv:1605.01157 \[hep-ph\]](#).
- [37] **KAGRA, Virgo, LIGO Scientific** Collaboration, R. Abbott et al., “Upper limits on the isotropic gravitational-wave background from Advanced LIGO and Advanced Virgo’s third observing run,” *Phys. Rev. D* **104** no. 2, (2021) 022004, [arXiv:2101.12130 \[gr-qc\]](#).
- [38] A. Sesana et al., “Unveiling the gravitational universe at μ -Hz frequencies,” *Exper. Astron.* **51** no. 3, (2021) 1333–1383, [arXiv:1908.11391 \[astro-ph.IM\]](#).
- [39] **LISA** Collaboration, P. Amaro-Seoane et al., “Laser Interferometer Space Antenna,” [arXiv:1702.00786 \[astro-ph.IM\]](#).
- [40] N. Seto, S. Kawamura, and T. Nakamura, “Possibility of direct measurement of the acceleration of the universe using 0.1-Hz band laser interferometer gravitational wave antenna in space,” *Phys. Rev. Lett.* **87** (2001) 221103, [arXiv:astro-ph/0108011](#).
- [41] V. Corbin and N. J. Cornish, “Detecting the cosmic gravitational wave background with the big bang observer,” *Class. Quant. Grav.* **23** (2006) 2435–2446, [arXiv:gr-qc/0512039](#).
- [42] M. Punturo et al., “The Einstein Telescope: A third-generation gravitational wave observatory,” *Class. Quant. Grav.* **27** (2010) 194002.
- [43] D. Reitze et al., “Cosmic Explorer: The U.S. Contribution to Gravitational-Wave Astronomy beyond LIGO,” *Bull. Am. Astron. Soc.* **51** no. 7, (2019) 035, [arXiv:1907.04833 \[astro-ph.IM\]](#).
- [44] **NANOGrav** Collaboration, G. Agazie et al., “The NANOGrav 15 yr Data Set: Evidence for a Gravitational-wave Background,” *Astrophys. J. Lett.* **951** no. 1, (2023) L8, [arXiv:2306.16213 \[astro-ph.HE\]](#).
- [45] J. Antoniadis et al., “The second data release from the European Pulsar Timing Array III. Search for gravitational wave signals,” [arXiv:2306.16214 \[astro-ph.HE\]](#).
- [46] D. J. Reardon et al., “Search for an Isotropic Gravitational-wave Background with the Parkes Pulsar Timing Array,” *Astrophys. J. Lett.* **951** no. 1, (2023) L6, [arXiv:2306.16215 \[astro-ph.HE\]](#).
- [47] H. Xu et al., “Searching for the Nano-Hertz Stochastic Gravitational Wave Background with the Chinese Pulsar Timing Array Data Release I,” *Res. Astron. Astrophys.* **23** no. 7, (2023) 075024, [arXiv:2306.16216 \[astro-ph.HE\]](#).
- [48] P. Binetruy, S. Lavignac, S. T. Petcov, and P. Ramond, “Quasidegenerate neutrinos from an Abelian family symmetry,” *Nucl. Phys. B* **496** (1997) 3–23, [arXiv:hep-ph/9610481](#).
- [49] N. F. Bell and R. R. Volkas, “Bottom up model for maximal muon-neutrino - tau-neutrino mixing,” *Phys. Rev. D* **63** (2001) 013006, [arXiv:hep-ph/0008177](#).
- [50] C. S. Lam, “A 2-3 symmetry in neutrino oscillations,” *Phys. Lett. B* **507** (2001) 214–218, [arXiv:hep-ph/0104116](#).
- [51] S. Choubey and W. Rodejohann, “A Flavor symmetry for quasi-degenerate neutrinos: $L(\mu) - L(\tau)$,” *Eur. Phys. J. C* **40** (2005) 259–268, [arXiv:hep-ph/0411190](#).
- [52] K. Asai, K. Hamaguchi, and N. Nagata, “Predictions for the neutrino parameters in the minimal gauged $U(1)_{L_\mu - L_\tau}$ model,” *Eur. Phys. J. C* **77** no. 11, (2017) 763, [arXiv:1705.00419 \[hep-ph\]](#).
- [53] S. N. Gninenko and N. V. Krasnikov, “The Muon anomalous magnetic moment and a new light gauge boson,” *Phys. Lett. B* **513** (2001) 119, [arXiv:hep-ph/0102222](#).
- [54] S. Baek, N. G. Deshpande, X. G. He, and P. Ko, “Muon anomalous $g-2$ and gauged $L(\mu) - L(\tau)$ models,” *Phys. Rev. D* **64** (2001) 055006, [arXiv:hep-ph/0104141](#).
- [55] E. Ma, D. P. Roy, and S. Roy, “Gauged $L(\mu) - L(\tau)$ with large muon anomalous magnetic moment and the bimaximal mixing of neutrinos,” *Phys. Lett. B* **525** (2002) 101–106, [arXiv:hep-ph/0110146](#).
- [56] T. Ota and W. Rodejohann, “Breaking of $L(\mu) - L(\tau)$ Flavor Symmetry, Lepton Flavor Violation and Leptogenesis,” *Phys. Lett. B* **639** (2006) 322–331, [arXiv:hep-ph/0605231](#).
- [57] J. Heeck and W. Rodejohann, “Gauged $L_\mu - L_\tau$ Symmetry at the Electroweak Scale,” *Phys. Rev. D* **84** (2011) 075007, [arXiv:1107.5238 \[hep-ph\]](#).

- [58] P. Foldenauer, “Light dark matter in a gauged $U(1)_{L_\mu-L_\tau}$ model,” *Phys. Rev. D* **99** no. 3, (2019) 035007, [arXiv:1808.03647 \[hep-ph\]](#).
- [59] M. Escudero, D. Hooper, G. Krnjaic, and M. Pierre, “Cosmology with A Very Light $L_\mu - L_\tau$ Gauge Boson,” *JHEP* **03** (2019) 071, [arXiv:1901.02010 \[hep-ph\]](#).
- [60] A. S. Joshipura, N. Mahajan, and K. M. Patel, “Generalised μ - τ symmetries and calculable gauge kinetic and mass mixing in $U(1)_{L_\mu-L_\tau}$ models,” *JHEP* **03** (2020) 001, [arXiv:1909.02331 \[hep-ph\]](#).
- [61] P. S. B. Dev, W. Rodejohann, X.-J. Xu, and Y. Zhang, “MUonE sensitivity to new physics explanations of the muon anomalous magnetic moment,” *JHEP* **05** (2020) 053, [arXiv:2002.04822 \[hep-ph\]](#).
- [62] Y. Zhang, Z. Yu, Q. Yang, M. Song, G. Li, and R. Ding, “Probing the $L_\mu - L_\tau$ gauge boson at electron colliders,” *Phys. Rev. D* **103** no. 1, (2021) 015008, [arXiv:2012.10893 \[hep-ph\]](#).
- [63] G.-y. Huang, F. S. Queiroz, and W. Rodejohann, “Gauged $L_\mu-L_\tau$ at a muon collider,” *Phys. Rev. D* **103** no. 9, (2021) 095005, [arXiv:2101.04956 \[hep-ph\]](#).
- [64] T. Araki, K. Asai, K. Honda, R. Kasuya, J. Sato, T. Shimomura, and M. J. S. Yang, “Resolving the Hubble tension in a $U(1)_{L_\mu-L_\tau}$ model with the Majoron,” *PTEP* **2021** no. 10, (2021) 103B05, [arXiv:2103.07167 \[hep-ph\]](#).
- [65] D. W. P. Amaral, D. G. Cerdeno, A. Cheek, and P. Foldenauer, “Confirming $U(1)_{L_\mu-L_\tau}$ as a solution for $(g-2)_\mu$ with neutrinos,” *Eur. Phys. J. C* **81** no. 10, (2021) 861, [arXiv:2104.03297 \[hep-ph\]](#).
- [66] A. J. Buras, A. Crivellin, F. Kirk, C. A. Manzari, and M. Montull, “Global analysis of leptophilic Z' bosons,” *JHEP* **06** (2021) 068, [arXiv:2104.07680 \[hep-ph\]](#).
- [67] D. Borah, A. Dasgupta, and D. Mahanta, “TeV scale resonant leptogenesis with $L_\mu-L_\tau$ gauge symmetry in light of the muon $g-2$,” *Phys. Rev. D* **104** no. 7, (2021) 075006, [arXiv:2106.14410 \[hep-ph\]](#).
- [68] M. Drees and W. Zhao, “ $U(1)_{L_\mu-L_\tau}$ for light dark matter, muon $g-2$, the 511 keV excess and the Hubble tension,” *Phys. Lett. B* **827** (2022) 136948, [arXiv:2107.14528 \[hep-ph\]](#).
- [69] T. Hapitas, D. Tuckler, and Y. Zhang, “General kinetic mixing in gauged $U(1)_{L_\mu-L_\tau}$ model for muon $g-2$ and dark matter,” *Phys. Rev. D* **105** no. 1, (2022) 016014, [arXiv:2108.12440 \[hep-ph\]](#).
- [70] K. Asai, K. Hamaguchi, N. Nagata, S.-Y. Tseng, and J. Wada, “Probing the $L_\mu-L_\tau$ gauge boson at the MUonE experiment,” *Phys. Rev. D* **106** no. 5, (2022) L051702, [arXiv:2109.10093 \[hep-ph\]](#).
- [71] Y. Cheng, X.-G. He, and J. Sun, “Widening the $U(1)_{L_\mu-L_\tau Z'}$ mass range for resolving the muon $g-2$ anomaly,” *Phys. Lett. B* **827** (2022) 136989, [arXiv:2112.09920 \[hep-ph\]](#).
- [72] J. Heeck and A. Thapa, “Explaining lepton-flavor non-universality and self-interacting dark matter with $L_\mu - L_\tau$,” *Eur. Phys. J. C* **82** no. 5, (2022) 480, [arXiv:2202.08854 \[hep-ph\]](#).
- [73] S. Eijima, M. Ibe, and K. Murai, “Muon $g-2$ and non-thermal leptogenesis in $U(1)_{L_\mu-L_\tau}$ model,” *JHEP* **05** (2023) 010, [arXiv:2303.09751 \[hep-ph\]](#).
- [74] C.-H. Chen, C.-W. Chiang, and C.-W. Su, “Compatibility of $CE\nu NS$ with muon $g-2$, W mass, and $R(D^{(*)})$ in a gauged $L_\mu - L_\tau$ with a scalar LQ,” [arXiv:2305.09256 \[hep-ph\]](#).
- [75] T. Araki, J. Heeck, and J. Kubo, “Vanishing Minors in the Neutrino Mass Matrix from Abelian Gauge Symmetries,” *JHEP* **07** (2012) 083, [arXiv:1203.4951 \[hep-ph\]](#).
- [76] J. Heeck, M. Lindner, W. Rodejohann, and S. Vogl, “Non-Standard Neutrino Interactions and Neutral Gauge Bosons,” *SciPost Phys.* **6** no. 3, (2019) 038, [arXiv:1812.04067 \[hep-ph\]](#).
- [77] P. Ballett, M. Hostert, S. Pascoli, Y. F. Perez-Gonzalez, Z. Tabrizi, and R. Zukanovich Funchal, “ Z' s in neutrino scattering at DUNE,” *Phys. Rev. D* **100** no. 5, (2019) 055012, [arXiv:1902.08579 \[hep-ph\]](#).
- [78] K. Asai, “Predictions for the neutrino parameters in the minimal model extended by linear combination of $U(1)_{L_e-L_\mu}$, $U(1)_{L_\mu-L_\tau}$ and $U(1)_{B-L}$ gauge symmetries,” *Eur. Phys. J. C* **80** no. 2, (2020) 76, [arXiv:1907.04042 \[hep-ph\]](#).
- [79] P. S. B. Dev, D. Kim, K. Sinha, and Y. Zhang, “New interference effects from light gauge bosons in neutrino-electron scattering,” *Phys. Rev. D* **104** no. 7, (2021) 075001, [arXiv:2105.09309 \[hep-ph\]](#).
- [80] M. Ardu and F. Kirk, “A viable $L_e - L_\mu$ model with $\mu \rightarrow e$ violation,” *Eur. Phys. J. C* **83** no. 5, (2023) 394, [arXiv:2205.02254 \[hep-ph\]](#).

- [81] P. Galison and A. Manohar, “TWO Z’s OR NOT TWO Z’s?,” *Phys. Lett. B* **136** (1984) 279–283.
- [82] B. Holdom, “Two U(1)’s and Epsilon Charge Shifts,” *Phys. Lett. B* **166** (1986) 196–198.
- [83] K. S. Babu, C. F. Kolda, and J. March-Russell, “Implications of generalized Z - Z-prime mixing,” *Phys. Rev. D* **57** (1998) 6788–6792, [arXiv:hep-ph/9710441](#).
- [84] M. Ibe, W. Nakano, and M. Suzuki, “Constraints on $L_\mu - L_\tau$ gauge interactions from rare kaon decay,” *Phys. Rev. D* **95** no. 5, (2017) 055022, [arXiv:1611.08460 \[hep-ph\]](#).
- [85] T. Araki, S. Hoshino, T. Ota, J. Sato, and T. Shimomura, “Detecting the $L_\mu - L_\tau$ gauge boson at Belle II,” *Phys. Rev. D* **95** no. 5, (2017) 055006, [arXiv:1702.01497 \[hep-ph\]](#).
- [86] P. Ilten, Y. Soreq, M. Williams, and W. Xue, “Serendipity in dark photon searches,” *JHEP* **06** (2018) 004, [arXiv:1801.04847 \[hep-ph\]](#).
- [87] M. Bauer, P. Foldenauer, and J. Jaeckel, “Hunting All the Hidden Photons,” *JHEP* **07** (2018) 094, [arXiv:1803.05466 \[hep-ph\]](#).
- [88] J. P. Leveille, “The Second Order Weak Correction to (G-2) of the Muon in Arbitrary Gauge Models,” *Nucl. Phys. B* **137** (1978) 63–76.
- [89] P. Fayet, “U-boson production in e+ e- annihilations, psi and Upsilon decays, and Light Dark Matter,” *Phys. Rev. D* **75** (2007) 115017, [arXiv:hep-ph/0702176](#).
- [90] X. Fan, T. G. Myers, B. A. D. Sukra, and G. Gabrielse, “Measurement of the Electron Magnetic Moment,” *Phys. Rev. Lett.* **130** no. 7, (2023) 071801, [arXiv:2209.13084 \[physics.atom-ph\]](#).
- [91] T. Aoyama, T. Kinoshita, and M. Nio, “Theory of the Anomalous Magnetic Moment of the Electron,” *Atoms* **7** no. 1, (2019) 28.
- [92] L. Morel, Z. Yao, P. Cladé, and S. Guellati-Khélifa, “Determination of the fine-structure constant with an accuracy of 81 parts per trillion,” *Nature* **588** no. 7836, (2020) 61–65.
- [93] R. H. Parker, C. Yu, W. Zhong, B. Estey, and H. Müller, “Measurement of the fine-structure constant as a test of the Standard Model,” *Science* **360** (2018) 191, [arXiv:1812.04130 \[physics.atom-ph\]](#).
- [94] **Muon g-2** Collaboration, B. Abi et al., “Measurement of the Positive Muon Anomalous Magnetic Moment to 0.46 ppm,” *Phys. Rev. Lett.* **126** no. 14, (2021) 141801, [arXiv:2104.03281 \[hep-ex\]](#).
- [95] **Muon g-2** Collaboration, D. P. Aguillard et al., “Measurement of the Positive Muon Anomalous Magnetic Moment to 0.20 ppm,” [arXiv:2308.06230 \[hep-ex\]](#).
- [96] **Muon g-2** Collaboration, G. W. Bennett et al., “Final Report of the Muon E821 Anomalous Magnetic Moment Measurement at BNL,” *Phys. Rev. D* **73** (2006) 072003, [arXiv:hep-ex/0602035](#).
- [97] T. Aoyama et al., “The anomalous magnetic moment of the muon in the Standard Model,” *Phys. Rept.* **887** (2020) 1–166, [arXiv:2006.04822 \[hep-ph\]](#).
- [98] S. Borsanyi et al., “Leading hadronic contribution to the muon magnetic moment from lattice QCD,” *Nature* **593** no. 7857, (2021) 51–55, [arXiv:2002.12347 \[hep-lat\]](#).
- [99] M. Cè et al., “Window observable for the hadronic vacuum polarization contribution to the muon g-2 from lattice QCD,” *Phys. Rev. D* **106** no. 11, (2022) 114502, [arXiv:2206.06582 \[hep-lat\]](#).
- [100] **Extended Twisted Mass** Collaboration, C. Alexandrou et al., “Lattice calculation of the short and intermediate time-distance hadronic vacuum polarization contributions to the muon magnetic moment using twisted-mass fermions,” *Phys. Rev. D* **107** no. 7, (2023) 074506, [arXiv:2206.15084 \[hep-lat\]](#).
- [101] **Fermilab Lattice, HPQCD,, MILC** Collaboration, A. Bazavov et al., “Light-quark connected intermediate-window contributions to the muon g-2 hadronic vacuum polarization from lattice QCD,” *Phys. Rev. D* **107** no. 11, (2023) 114514, [arXiv:2301.08274 \[hep-lat\]](#).
- [102] T. Blum et al., “An update of Euclidean windows of the hadronic vacuum polarization,” [arXiv:2301.08696 \[hep-lat\]](#).
- [103] H. Wittig, “Progress on $(g - 2)_\mu$ from Lattice QCD,” in *57th Rencontres de Moriond on Electroweak Interactions and Unified Theories*. 6, 2023. [arXiv:2306.04165 \[hep-ph\]](#).
- [104] **DELPHI** Collaboration, J. Abdallah et al., “Study of tau-pair production in photon-photon collisions at LEP and limits on the anomalous electromagnetic moments of the tau lepton,” *Eur.*

- [Phys. J. C](#) **35** (2004) 159–170, [arXiv:hep-ex/0406010](#).
- [105] **ATLAS** Collaboration, “Observation of the $\gamma\gamma \rightarrow \tau\tau$ process in Pb+Pb collisions and constraints on the τ -lepton anomalous magnetic moment with the ATLAS detector,” [arXiv:2204.13478](#) [[hep-ex](#)].
- [106] **CMS** Collaboration, “Observation of τ lepton pair production in ultraperipheral lead-lead collisions at $\sqrt{s_{NN}} = 5.02$ TeV,” [arXiv:2206.05192](#) [[nucl-ex](#)].
- [107] G. A. Gonzalez-Sprinberg, A. Santamaria, and J. Vidal, “Model independent bounds on the tau lepton electromagnetic and weak magnetic moments,” [Nucl. Phys. B](#) **582** (2000) 3–18, [arXiv:hep-ph/0002203](#).
- [108] U. Haisch, L. Schnell, and J. Weiss, “LHC tau-pair production constraints on a_τ and d_τ ,” [arXiv:2307.14133](#) [[hep-ph](#)].
- [109] J. S. Schwinger, “On Quantum electrodynamics and the magnetic moment of the electron,” [Phys. Rev.](#) **73** (1948) 416–417.
- [110] W. Altmannshofer, S. Gori, M. Pospelov, and I. Yavin, “Neutrino Trident Production: A Powerful Probe of New Physics with Neutrino Beams,” [Phys. Rev. Lett.](#) **113** (2014) 091801, [arXiv:1406.2332](#) [[hep-ph](#)].
- [111] **CHARM-II** Collaboration, D. Geiregat *et al.*, “First observation of neutrino trident production,” [Phys. Lett. B](#) **245** (1990) 271–275.
- [112] **CCFR** Collaboration, S. R. Mishra *et al.*, “Neutrino tridents and W Z interference,” [Phys. Rev. Lett.](#) **66** (1991) 3117–3120.
- [113] **NuTeV** Collaboration, T. Adams *et al.*, “Neutrino trident production from NuTeV,” in *29th International Conference on High-Energy Physics*, pp. 631–634. 7, 1998. [arXiv:hep-ex/9811012](#).
- [114] W. Altmannshofer, S. Gori, S. Profumo, and F. S. Queiroz, “Explaining dark matter and B decay anomalies with an $L_\mu - L_\tau$ model,” [JHEP](#) **12** (2016) 106, [arXiv:1609.04026](#) [[hep-ph](#)].
- [115] **NA64** Collaboration, Y. M. Andreev *et al.*, “Search for a light Z' in the L_μ - L_τ scenario with the NA64-e experiment at CERN,” [Phys. Rev. D](#) **106** no. 3, (2022) 032015, [arXiv:2206.03101](#) [[hep-ex](#)].
- [116] **LSND** Collaboration, L. B. Auerbach *et al.*, “Measurement of electron - neutrino - electron elastic scattering,” [Phys. Rev. D](#) **63** (2001) 112001, [arXiv:hep-ex/0101039](#).
- [117] **TEXONO** Collaboration, M. Deniz *et al.*, “Measurement of $\text{Nu}(e)\text{-bar}$ -Electron Scattering Cross-Section with a CsI(Tl) Scintillating Crystal Array at the Kuo-Sheng Nuclear Power Reactor,” [Phys. Rev. D](#) **81** (2010) 072001, [arXiv:0911.1597](#) [[hep-ex](#)].
- [118] S. Bilmis, I. Turan, T. M. Aliev, M. Deniz, L. Singh, and H. T. Wong, “Constraints on Dark Photon from Neutrino-Electron Scattering Experiments,” [Phys. Rev. D](#) **92** no. 3, (2015) 033009, [arXiv:1502.07763](#) [[hep-ph](#)].
- [119] M. B. Wise and Y. Zhang, “Lepton Flavorful Fifth Force and Depth-dependent Neutrino Matter Interactions,” [JHEP](#) **06** (2018) 053, [arXiv:1803.00591](#) [[hep-ph](#)].
- [120] P. S. B. Dev *et al.*, “Neutrino Non-Standard Interactions: A Status Report,” [arXiv:1907.00991](#) [[hep-ph](#)].
- [121] **IceCube** Collaboration, R. Abbasi *et al.*, “Non-standard neutrino interactions in IceCube,” [PoS EPS-HEP2021](#) (2022) 245.
- [122] **(IceCube Collaboration)***, **IceCube** Collaboration, R. Abbasi *et al.*, “All-flavor constraints on nonstandard neutrino interactions and generalized matter potential with three years of IceCube DeepCore data,” [Phys. Rev. D](#) **104** no. 7, (2021) 072006, [arXiv:2106.07755](#) [[hep-ex](#)].
- [123] **ANTARES** Collaboration, A. Albert *et al.*, “Search for non-standard neutrino interactions with 10 years of ANTARES data,” [JHEP](#) **07** (2022) 048, [arXiv:2112.14517](#) [[hep-ex](#)].
- [124] **Super-Kamiokande** Collaboration, G. Mitsuka *et al.*, “Study of Non-Standard Neutrino Interactions with Atmospheric Neutrino Data in Super-Kamiokande I and II,” [Phys. Rev. D](#) **84** (2011) 113008, [arXiv:1109.1889](#) [[hep-ex](#)].
- [125] M. R. Buckley, D. Hooper, J. Kopp, and E. Neil, “Light Z' Bosons at the Tevatron,” [Phys. Rev. D](#) **83** (2011) 115013, [arXiv:1103.6035](#) [[hep-ph](#)].

- [126] **ALEPH** Collaboration, D. Buskulic et al., “Study of the four fermion final state at the Z resonance,” *Z. Phys. C* **66** (1995) 3–18.
- [127] **DELPHI** Collaboration, J. Abdallah et al., “Photon events with missing energy in e^+e^- collisions at $s^{*}(1/2) = 130\text{-GeV}$ to 209-GeV ,” *Eur. Phys. J. C* **38** (2005) 395–411, [arXiv:hep-ex/0406019](#).
- [128] **DELPHI** Collaboration, J. Abdallah et al., “Search for one large extra dimension with the DELPHI detector at LEP,” *Eur. Phys. J. C* **60** (2009) 17–23, [arXiv:0901.4486 \[hep-ex\]](#).
- [129] P. J. Fox, R. Harnik, J. Kopp, and Y. Tsai, “LEP Shines Light on Dark Matter,” *Phys. Rev. D* **84** (2011) 014028, [arXiv:1103.0240 \[hep-ph\]](#).
- [130] **ATLAS** Collaboration, “Search for a new Z' gauge boson in 4μ events with the ATLAS experiment,”.
- [131] **CMS** Collaboration, A. M. Sirunyan et al., “Search for an $L_\mu - L_\tau$ gauge boson using $Z \rightarrow 4\mu$ events in proton-proton collisions at $\sqrt{s} = 13$ TeV,” *Phys. Lett. B* **792** (2019) 345–368, [arXiv:1808.03684 \[hep-ex\]](#).
- [132] **CMS** Collaboration, A. M. Sirunyan et al., “Measurements of the $pp \rightarrow ZZ$ production cross section and the $Z \rightarrow 4\ell$ branching fraction, and constraints on anomalous triple gauge couplings at $\sqrt{s} = 13$ TeV,” *Eur. Phys. J. C* **78** (2018) 165, [arXiv:1709.08601 \[hep-ex\]](#). [Erratum: *Eur.Phys.J.C* **78**, 515 (2018)].
- [133] **CMS** Collaboration, A. M. Sirunyan et al., “Search for electroweak production of charginos and neutralinos in multilepton final states in proton-proton collisions at $\sqrt{s} = 13$ TeV,” *JHEP* **03** (2018) 166, [arXiv:1709.05406 \[hep-ex\]](#).
- [134] M. Drees, M. Shi, and Z. Zhang, “Constraints on $U(1)_{L_\mu-L_\tau}$ from LHC Data,” *Phys. Lett. B* **791** (2019) 130–136, [arXiv:1811.12446 \[hep-ph\]](#).
- [135] **BaBar** Collaboration, J. P. Lees et al., “Search for a muonic dark force at BABAR,” *Phys. Rev. D* **94** no. 1, (2016) 011102, [arXiv:1606.03501 \[hep-ex\]](#).
- [136] **Belle** Collaboration, T. Czank et al., “Search for $Z' \rightarrow \mu^+\mu^-$ in the $L_\mu-L_\tau$ gauge-symmetric model at Belle,” *Phys. Rev. D* **106** no. 1, (2022) 012003, [arXiv:2109.08596 \[hep-ex\]](#).
- [137] **LHCb** Collaboration, R. Aaij et al., “Search for $A' \rightarrow \mu^+\mu^-$ Decays,” *Phys. Rev. Lett.* **124** no. 4, (2020) 041801, [arXiv:1910.06926 \[hep-ex\]](#).
- [138] **Belle-II** Collaboration, I. Adachi et al., “Search for an Invisible Z' in a Final State with Two Muons and Missing Energy at Belle II,” *Phys. Rev. Lett.* **130** no. 23, (2023) 231801, [arXiv:2212.03066 \[hep-ex\]](#).
- [139] **Belle-II** Collaboration, I. Adachi et al., “Search for a $\tau^+\tau^-$ resonance in $e^+e^- \rightarrow \mu^+\mu^-\tau^+\tau^-$ events with the Belle II experiment,” [arXiv:2306.12294 \[hep-ex\]](#).
- [140] **CMS** Collaboration, “Search for the Z boson decay to $\tau^+\tau^-\mu^+\mu^-$ in proton-proton collisions at $\sqrt{s} = 13$ TeV,”.
- [141] C. Cheung, J. T. Ruderman, L.-T. Wang, and I. Yavin, “Kinetic Mixing as the Origin of Light Dark Scales,” *Phys. Rev. D* **80** (2009) 035008, [arXiv:0902.3246 \[hep-ph\]](#).
- [142] M. Bauer and P. Foldenauer, “Consistent Theory of Kinetic Mixing and the Higgs Low-Energy Theorem,” *Phys. Rev. Lett.* **129** no. 17, (2022) 171801, [arXiv:2207.00023 \[hep-ph\]](#).
- [143] Y. Hosseini and M. M. Najafabadi, “Unitarity constraints and collider searches for dark photons,” *Phys. Rev. D* **106** no. 1, (2022) 015028, [arXiv:2202.10058 \[hep-ph\]](#).
- [144] A. Das, T. Nomura, and T. Shimomura, “Multi muon/anti-muon signals via productions of gauge and scalar bosons in a $U(1)_{L_\mu-L_\tau}$ model at muonic colliders,” [arXiv:2212.11674 \[hep-ph\]](#).
- [145] J. Sun, F. Huang, and X.-G. He, “Muon collider signatures for a Z' with a maximal $\mu - \tau$ coupling in $U(1)_{L_\mu-L_\tau}$,” [arXiv:2307.00531 \[hep-ph\]](#).
- [146] S. Jana and S. Klett, “Muonic Force and Neutrino Non-Standard Interactions at Muon Colliders,” [arXiv:2308.07375 \[hep-ph\]](#).
- [147] M. Moretti, T. Ohl, and J. Reuter, “O’Mega: An Optimizing matrix element generator,” [arXiv:hep-ph/0102195](#).
- [148] W. Kilian, T. Ohl, and J. Reuter, “WHIZARD: Simulating Multi-Particle Processes at LHC and ILC,” *Eur. Phys. J. C* **71** (2011) 1742, [arXiv:0708.4233 \[hep-ph\]](#).

- [149] J. Alwall, R. Frederix, S. Frixione, V. Hirschi, F. Maltoni, O. Mattelaer, H. S. Shao, T. Stelzer, P. Torrielli, and M. Zaro, “The automated computation of tree-level and next-to-leading order differential cross sections, and their matching to parton shower simulations,” *JHEP* **07** (2014) 079, [arXiv:1405.0301 \[hep-ph\]](#).
- [150] N. D. Christensen, C. Duhr, B. Fuks, J. Reuter, and C. Speckner, “Introducing an interface between WHIZARD and FeynRules,” *Eur. Phys. J. C* **72** (2012) 1990, [arXiv:1010.3251 \[hep-ph\]](#).
- [151] A. Denig, “The Radiative return: A Review of experimental results,” *Nucl. Phys. B Proc. Suppl.* **162** (2006) 81–89, [arXiv:hep-ex/0611024](#).
- [152] V. M. Budnev, I. F. Ginzburg, G. V. Meledin, and V. G. Serbo, “The Two photon particle production mechanism. Physical problems. Applications. Equivalent photon approximation,” *Phys. Rept.* **15** (1975) 181–281.
- [153] S. Frixione, M. L. Mangano, P. Nason, and G. Ridolfi, “Improving the Weizsacker-Williams approximation in electron - proton collisions,” *Phys. Lett. B* **319** (1993) 339–345, [arXiv:hep-ph/9310350](#).
- [154] T. Han, D. Liu, I. Low, and X. Wang, “Electroweak couplings of the Higgs boson at a multi-TeV muon collider,” *Phys. Rev. D* **103** no. 1, (2021) 013002, [arXiv:2008.12204 \[hep-ph\]](#).
- [155] **ALEPH, DELPHI, L3, OPAL, SLD, LEP Electroweak Working Group, SLD Electroweak Group, SLD Heavy Flavour Group** Collaboration, S. Schael et al., “Precision electroweak measurements on the Z resonance,” *Phys. Rept.* **427** (2006) 257–454, [arXiv:hep-ex/0509008](#).
- [156] J. Li and A. G. Williams, “Tau reconstruction methods at an electron-positron collider in the search for new physics,” *Phys. Rev. D* **93** no. 7, (2016) 075019, [arXiv:1508.05675 \[hep-ph\]](#).
- [157] D. Yu, M. Ruan, V. Boudry, H. Videau, J.-C. Brient, Z. Wu, Q. Ouyang, Y. Xu, and X. Chen, “The measurement of the $H \rightarrow \tau\tau$ signal strength in the future e^+e^- Higgs factories,” *Eur. Phys. J. C* **80** no. 1, (2020) 7.
- [158] F. del Aguila, M. Chala, J. Santiago, and Y. Yamamoto, “Collider limits on leptophilic interactions,” *JHEP* **03** (2015) 059, [arXiv:1411.7394 \[hep-ph\]](#).
- [159] R. Jinno and M. Takimoto, “Probing a classically conformal B-L model with gravitational waves,” *Phys. Rev. D* **95** no. 1, (2017) 015020, [arXiv:1604.05035 \[hep-ph\]](#).
- [160] W. Chao, W.-F. Cui, H.-K. Guo, and J. Shu, “Gravitational wave imprint of new symmetry breaking,” *Chin. Phys. C* **44** no. 12, (2020) 123102, [arXiv:1707.09759 \[hep-ph\]](#).
- [161] V. Brdar, A. J. Helmboldt, and J. Kubo, “Gravitational Waves from First-Order Phase Transitions: LIGO as a Window to Unexplored Seesaw Scales,” *JCAP* **02** (2019) 021, [arXiv:1810.12306 \[hep-ph\]](#).
- [162] C. Marzo, L. Marzola, and V. Vaskonen, “Phase transition and vacuum stability in the classically conformal B–L model,” *Eur. Phys. J. C* **79** no. 7, (2019) 601, [arXiv:1811.11169 \[hep-ph\]](#).
- [163] T. Hasegawa, N. Okada, and O. Seto, “Gravitational waves from the minimal gauged $U(1)_{B-L}$ model,” *Phys. Rev. D* **99** no. 9, (2019) 095039, [arXiv:1904.03020 \[hep-ph\]](#).
- [164] J. Ellis, M. Lewicki, and V. Vaskonen, “Updated predictions for gravitational waves produced in a strongly supercooled phase transition,” *JCAP* **11** (2020) 020, [arXiv:2007.15586 \[astro-ph.CO\]](#).
- [165] P. Huang and K.-P. Xie, “Leptogenesis triggered by a first-order phase transition,” *JHEP* **09** (2022) 052, [arXiv:2206.04691 \[hep-ph\]](#).
- [166] A. Dasgupta, P. S. B. Dev, A. Ghoshal, and A. Mazumdar, “Gravitational wave pathway to testable leptogenesis,” *Phys. Rev. D* **106** no. 7, (2022) 075027, [arXiv:2206.07032 \[hep-ph\]](#).
- [167] A. Chikhaballi, K. Kowalska, and E. M. Sessolo, “Naturally small neutrino mass with asymptotic safety and gravitational-wave signatures,” [arXiv:2308.06114 \[hep-ph\]](#).
- [168] P. Athron, C. Balázs, A. Fowlie, L. Morris, and L. Wu, “Cosmological phase transitions: from perturbative particle physics to gravitational waves,” [arXiv:2305.02357 \[hep-ph\]](#).
- [169] E. Gildener and S. Weinberg, “Symmetry Breaking and Scalar Bosons,” *Phys. Rev. D* **13** (1976) 3333.
- [170] M. Sher, “Electroweak Higgs Potentials and Vacuum Stability,” *Phys. Rept.* **179** (1989) 273–418.

- [171] K. A. Meissner and H. Nicolai, “Renormalization Group and Effective Potential in Classically Conformal Theories,” *Acta Phys. Polon. B* **40** (2009) 2737–2752, [arXiv:0809.1338 \[hep-th\]](#).
- [172] H. H. Patel and M. J. Ramsey-Musolf, “Baryon Washout, Electroweak Phase Transition, and Perturbation Theory,” *JHEP* **07** (2011) 029, [arXiv:1101.4665 \[hep-ph\]](#).
- [173] C. Wainwright, S. Profumo, and M. J. Ramsey-Musolf, “Gravity Waves from a Cosmological Phase Transition: Gauge Artifacts and Daisy Resummations,” *Phys. Rev. D* **84** (2011) 023521, [arXiv:1104.5487 \[hep-ph\]](#).
- [174] M. Garny and T. Konstandin, “On the gauge dependence of vacuum transitions at finite temperature,” *JHEP* **07** (2012) 189, [arXiv:1205.3392 \[hep-ph\]](#).
- [175] C.-W. Chiang and E. Senaha, “On gauge dependence of gravitational waves from a first-order phase transition in classical scale-invariant $U(1)'$ models,” *Phys. Lett. B* **774** (2017) 489–493, [arXiv:1707.06765 \[hep-ph\]](#).
- [176] J. Löfgren, M. J. Ramsey-Musolf, P. Schicho, and T. V. I. Tenkanen, “Nucleation at Finite Temperature: A Gauge-Invariant Perturbative Framework,” *Phys. Rev. Lett.* **130** no. 25, (2023) 251801, [arXiv:2112.05472 \[hep-ph\]](#).
- [177] M. Hashimoto, S. Iso, and Y. Orikasa, “Radiative symmetry breaking from flat potential in various $U(1)'$ models,” *Phys. Rev. D* **89** no. 5, (2014) 056010, [arXiv:1401.5944 \[hep-ph\]](#).
- [178] F. Staub, “SARAH,” [arXiv:0806.0538 \[hep-ph\]](#).
- [179] P. B. Arnold and O. Espinosa, “The Effective potential and first order phase transitions: Beyond leading-order,” *Phys. Rev. D* **47** (1993) 3546, [arXiv:hep-ph/9212235](#). [Erratum: *Phys.Rev.D* 50, 6662 (1994)].
- [180] S. R. Coleman, “The Fate of the False Vacuum. 1. Semiclassical Theory,” *Phys. Rev. D* **15** (1977) 2929–2936. [Erratum: *Phys.Rev.D* 16, 1248 (1977)].
- [181] A. D. Linde, “On the Vacuum Instability and the Higgs Meson Mass,” *Phys. Lett. B* **70** (1977) 306–308.
- [182] A. D. Linde, “Decay of the False Vacuum at Finite Temperature,” *Nucl. Phys. B* **216** (1983) 421. [Erratum: *Nucl.Phys.B* 223, 544 (1983)].
- [183] S. R. Coleman, V. Glaser, and A. Martin, “Action Minima Among Solutions to a Class of Euclidean Scalar Field Equations,” *Commun. Math. Phys.* **58** (1978) 211–221.
- [184] J. R. Espinosa, “A Fresh Look at the Calculation of Tunneling Actions,” *JCAP* **07** (2018) 036, [arXiv:1805.03680 \[hep-th\]](#).
- [185] D. Croon, O. Gould, P. Schicho, T. V. I. Tenkanen, and G. White, “Theoretical uncertainties for cosmological first-order phase transitions,” *JHEP* **04** (2021) 055, [arXiv:2009.10080 \[hep-ph\]](#).
- [186] K. Saikawa and S. Shirai, “Primordial gravitational waves, precisely: The role of thermodynamics in the Standard Model,” *JCAP* **05** (2018) 035, [arXiv:1803.01038 \[hep-ph\]](#).
- [187] J. Ellis, M. Lewicki, and J. M. No, “On the Maximal Strength of a First-Order Electroweak Phase Transition and its Gravitational Wave Signal,” *JCAP* **04** (2019) 003, [arXiv:1809.08242 \[hep-ph\]](#).
- [188] A. H. Guth and S. H. H. Tye, “Phase Transitions and Magnetic Monopole Production in the Very Early Universe,” *Phys. Rev. Lett.* **44** (1980) 631. [Erratum: *Phys.Rev.Lett.* 44, 963 (1980)].
- [189] A. H. Guth and E. J. Weinberg, “Cosmological Consequences of a First Order Phase Transition in the $SU(5)$ Grand Unified Model,” *Phys. Rev. D* **23** (1981) 876.
- [190] A. H. Guth and E. J. Weinberg, “Could the Universe Have Recovered from a Slow First Order Phase Transition?,” *Nucl. Phys. B* **212** (1983) 321–364.
- [191] K. Enqvist, J. Ignatius, K. Kajantie, and K. Rummukainen, “Nucleation and bubble growth in a first order cosmological electroweak phase transition,” *Phys. Rev. D* **45** (1992) 3415–3428.
- [192] M. S. Turner, E. J. Weinberg, and L. M. Widrow, “Bubble nucleation in first order inflation and other cosmological phase transitions,” *Phys. Rev. D* **46** (1992) 2384–2403.
- [193] J. R. Espinosa, T. Konstandin, J. M. No, and M. Quiros, “Some Cosmological Implications of Hidden Sectors,” *Phys. Rev. D* **78** (2008) 123528, [arXiv:0809.3215 \[hep-ph\]](#).
- [194] I. Baldes and M. O. Olea-Romacho, “Primordial black holes as dark matter: Interferometric tests of phase transition origin,” [arXiv:2307.11639 \[hep-ph\]](#).

- [195] E. Di Valentino, O. Mena, S. Pan, L. Visinelli, W. Yang, A. Melchiorri, D. F. Mota, A. G. Riess, and J. Silk, “In the realm of the Hubble tension—a review of solutions,” *Class. Quant. Grav.* **38** no. 15, (2021) 153001, [arXiv:2103.01183 \[astro-ph.CO\]](#).
- [196] A. Kosowsky, M. S. Turner, and R. Watkins, “Gravitational radiation from colliding vacuum bubbles,” *Phys. Rev. D* **45** (1992) 4514–4535.
- [197] A. Kosowsky, M. S. Turner, and R. Watkins, “Gravitational waves from first order cosmological phase transitions,” *Phys. Rev. Lett.* **69** (1992) 2026–2029.
- [198] A. Kosowsky and M. S. Turner, “Gravitational radiation from colliding vacuum bubbles: envelope approximation to many bubble collisions,” *Phys. Rev. D* **47** (1993) 4372–4391, [arXiv:astro-ph/9211004](#).
- [199] M. Kamionkowski, A. Kosowsky, and M. S. Turner, “Gravitational radiation from first order phase transitions,” *Phys. Rev. D* **49** (1994) 2837–2851, [arXiv:astro-ph/9310044](#).
- [200] C. Caprini, R. Durrer, and G. Servant, “Gravitational wave generation from bubble collisions in first-order phase transitions: An analytic approach,” *Phys. Rev. D* **77** (2008) 124015, [arXiv:0711.2593 \[astro-ph\]](#).
- [201] S. J. Huber and T. Konstandin, “Gravitational Wave Production by Collisions: More Bubbles,” *JCAP* **09** (2008) 022, [arXiv:0806.1828 \[hep-ph\]](#).
- [202] D. J. Weir, “Revisiting the envelope approximation: gravitational waves from bubble collisions,” *Phys. Rev. D* **93** no. 12, (2016) 124037, [arXiv:1604.08429 \[astro-ph.CO\]](#).
- [203] R. Jinno and M. Takimoto, “Gravitational waves from bubble dynamics: Beyond the Envelope,” *JCAP* **01** (2019) 060, [arXiv:1707.03111 \[hep-ph\]](#).
- [204] R. Jinno, T. Konstandin, and M. Takimoto, “Relativistic bubble collisions—a closer look,” *JCAP* **09** (2019) 035, [arXiv:1906.02588 \[hep-ph\]](#).
- [205] M. Lewicki and V. Vaskonen, “Gravitational wave spectra from strongly supercooled phase transitions,” *Eur. Phys. J. C* **80** no. 11, (2020) 1003, [arXiv:2007.04967 \[astro-ph.CO\]](#).
- [206] A. Megevand and F. A. Membiela, “Gravitational waves from bubble walls,” *JCAP* **10** (2021) 073, [arXiv:2108.05510 \[astro-ph.CO\]](#).
- [207] M. Hindmarsh, S. J. Huber, K. Rummukainen, and D. J. Weir, “Gravitational waves from the sound of a first order phase transition,” *Phys. Rev. Lett.* **112** (2014) 041301, [arXiv:1304.2433 \[hep-ph\]](#).
- [208] J. T. Giblin, Jr. and J. B. Mertens, “Vacuum Bubbles in the Presence of a Relativistic Fluid,” *JHEP* **12** (2013) 042, [arXiv:1310.2948 \[hep-th\]](#).
- [209] J. T. Giblin and J. B. Mertens, “Gravitational radiation from first-order phase transitions in the presence of a fluid,” *Phys. Rev. D* **90** no. 2, (2014) 023532, [arXiv:1405.4005 \[astro-ph.CO\]](#).
- [210] M. Hindmarsh, S. J. Huber, K. Rummukainen, and D. J. Weir, “Numerical simulations of acoustically generated gravitational waves at a first order phase transition,” *Phys. Rev. D* **92** no. 12, (2015) 123009, [arXiv:1504.03291 \[astro-ph.CO\]](#).
- [211] M. Hindmarsh, “Sound shell model for acoustic gravitational wave production at a first-order phase transition in the early Universe,” *Phys. Rev. Lett.* **120** no. 7, (2018) 071301, [arXiv:1608.04735 \[astro-ph.CO\]](#).
- [212] M. Hindmarsh, S. J. Huber, K. Rummukainen, and D. J. Weir, “Shape of the acoustic gravitational wave power spectrum from a first order phase transition,” *Phys. Rev. D* **96** no. 10, (2017) 103520, [arXiv:1704.05871 \[astro-ph.CO\]](#). [Erratum: *Phys.Rev.D* 101, 089902 (2020)].
- [213] M. Hindmarsh and M. Hijazi, “Gravitational waves from first order cosmological phase transitions in the Sound Shell Model,” *JCAP* **12** (2019) 062, [arXiv:1909.10040 \[astro-ph.CO\]](#).
- [214] C. Caprini and R. Durrer, “Gravitational waves from stochastic relativistic sources: Primordial turbulence and magnetic fields,” *Phys. Rev. D* **74** (2006) 063521, [arXiv:astro-ph/0603476](#).
- [215] T. Kahniashvili, A. Kosowsky, G. Gogoberidze, and Y. Maravin, “Detectability of Gravitational Waves from Phase Transitions,” *Phys. Rev. D* **78** (2008) 043003, [arXiv:0806.0293 \[astro-ph\]](#).
- [216] T. Kahniashvili, L. Campanelli, G. Gogoberidze, Y. Maravin, and B. Ratra, “Gravitational Radiation from Primordial Helical Inverse Cascade MHD Turbulence,” *Phys. Rev. D* **78** (2008) 123006, [arXiv:0809.1899 \[astro-ph\]](#). [Erratum: *Phys.Rev.D* 79, 109901 (2009)].

- [217] T. Kahniashvili, L. Kisslinger, and T. Stevens, “Gravitational Radiation Generated by Magnetic Fields in Cosmological Phase Transitions,” *Phys. Rev. D* **81** (2010) 023004, [arXiv:0905.0643 \[astro-ph.CO\]](#).
- [218] C. Caprini, R. Durrer, and G. Servant, “The stochastic gravitational wave background from turbulence and magnetic fields generated by a first-order phase transition,” *JCAP* **12** (2009) 024, [arXiv:0909.0622 \[astro-ph.CO\]](#).
- [219] L. Kisslinger and T. Kahniashvili, “Polarized Gravitational Waves from Cosmological Phase Transitions,” *Phys. Rev. D* **92** no. 4, (2015) 043006, [arXiv:1505.03680 \[astro-ph.CO\]](#).
- [220] A. Roper Pol, S. Mandal, A. Brandenburg, T. Kahniashvili, and A. Kosowsky, “Numerical simulations of gravitational waves from early-universe turbulence,” *Phys. Rev. D* **102** no. 8, (2020) 083512, [arXiv:1903.08585 \[astro-ph.CO\]](#).
- [221] P. Athron, C. Balázs, and L. Morris, “Supercool subtleties of cosmological phase transitions,” *JCAP* **03** (2023) 006, [arXiv:2212.07559 \[hep-ph\]](#).
- [222] M. Lewicki, M. Merchand, and M. Zych, “Electroweak bubble wall expansion: gravitational waves and baryogenesis in Standard Model-like thermal plasma,” *JHEP* **02** (2022) 017, [arXiv:2111.02393 \[astro-ph.CO\]](#).
- [223] P. J. Steinhardt, “Relativistic Detonation Waves and Bubble Growth in False Vacuum Decay,” *Phys. Rev. D* **25** (1982) 2074.
- [224] J. R. Espinosa, T. Konstandin, J. M. No, and G. Servant, “Energy Budget of Cosmological First-order Phase Transitions,” *JCAP* **06** (2010) 028, [arXiv:1004.4187 \[hep-ph\]](#).
- [225] J. Ellis, M. Lewicki, J. M. No, and V. Vaskonen, “Gravitational wave energy budget in strongly supercooled phase transitions,” *JCAP* **06** (2019) 024, [arXiv:1903.09642 \[hep-ph\]](#).
- [226] C. Caprini et al., “Science with the space-based interferometer eLISA. II: Gravitational waves from cosmological phase transitions,” *JCAP* **04** (2016) 001, [arXiv:1512.06239 \[astro-ph.CO\]](#).
- [227] K. Schmitz, “New Sensitivity Curves for Gravitational-Wave Signals from Cosmological Phase Transitions,” *JHEP* **01** (2021) 097, [arXiv:2002.04615 \[hep-ph\]](#).
- [228] T.-H. Yeh, J. Shelton, K. A. Olive, and B. D. Fields, “Probing physics beyond the standard model: limits from BBN and the CMB independently and combined,” *JCAP* **10** (2022) 046, [arXiv:2207.13133 \[astro-ph.CO\]](#).
- [229] C. Caprini and D. G. Figueroa, “Cosmological Backgrounds of Gravitational Waves,” *Class. Quant. Grav.* **35** no. 16, (2018) 163001, [arXiv:1801.04268 \[astro-ph.CO\]](#).
- [230] A. Weltman et al., “Fundamental physics with the Square Kilometre Array,” *Publ. Astron. Soc. Austral.* **37** (2020) e002, [arXiv:1810.02680 \[astro-ph.CO\]](#).
- [231] J. Garcia-Bellido, H. Murayama, and G. White, “Exploring the early Universe with Gaia and Theia,” *JCAP* **12** no. 12, (2021) 023, [arXiv:2104.04778 \[hep-ph\]](#).
- [232] **MAGIS-100** Collaboration, M. Abe et al., “Matter-wave Atomic Gradiometer Interferometric Sensor (MAGIS-100),” *Quantum Sci. Technol.* **6** no. 4, (2021) 044003, [arXiv:2104.02835 \[physics.atom-ph\]](#).
- [233] L. Badurina et al., “AION: An Atom Interferometer Observatory and Network,” *JCAP* **05** (2020) 011, [arXiv:1911.11755 \[astro-ph.CO\]](#).
- [234] **AEDGE** Collaboration, Y. A. El-Neaj et al., “AEDGE: Atomic Experiment for Dark Matter and Gravity Exploration in Space,” *EPJ Quant. Technol.* **7** (2020) 6, [arXiv:1908.00802 \[gr-qc\]](#).
- [235] **TianQin** Collaboration, J. Luo et al., “TianQin: a space-borne gravitational wave detector,” *Class. Quant. Grav.* **33** no. 3, (2016) 035010, [arXiv:1512.02076 \[astro-ph.IM\]](#).
- [236] W.-H. Ruan, Z.-K. Guo, R.-G. Cai, and Y.-Z. Zhang, “Taiji program: Gravitational-wave sources,” *Int. J. Mod. Phys. A* **35** no. 17, (2020) 2050075, [arXiv:1807.09495 \[gr-qc\]](#).
- [237] N. Aggarwal et al., “Challenges and opportunities of gravitational-wave searches at MHz to GHz frequencies,” *Living Rev. Rel.* **24** no. 1, (2021) 4, [arXiv:2011.12414 \[gr-qc\]](#).
- [238] A. Berlin, D. Blas, R. Tito D’Agnolo, S. A. R. Ellis, R. Harnik, Y. Kahn, and J. Schütte-Engel, “Detecting high-frequency gravitational waves with microwave cavities,” *Phys. Rev. D* **105** no. 11, (2022) 116011, [arXiv:2112.11465 \[hep-ph\]](#).

- [239] N. Herman, L. Lehoucq, and A. Fúzfá, “Electromagnetic Antennas for the Resonant Detection of the Stochastic Gravitational Wave Background,” [arXiv:2203.15668 \[gr-qc\]](#).
- [240] T. Bringmann, V. Domcke, E. Fuchs, and J. Kopp, “High-frequency gravitational wave detection via optical frequency modulation,” [Phys. Rev. D](#) **108** no. 6, (2023) L061303, [arXiv:2304.10579 \[hep-ph\]](#).
- [241] B. Allen, “The Stochastic gravity wave background: Sources and detection,” in [Les Houches School of Physics: Astrophysical Sources of Gravitational Radiation](#), pp. 373–417. 4, 1996. [arXiv:gr-qc/9604033](#).
- [242] B. Allen and J. D. Romano, “Detecting a stochastic background of gravitational radiation: Signal processing strategies and sensitivities,” [Phys. Rev. D](#) **59** (1999) 102001, [arXiv:gr-qc/9710117](#).
- [243] M. Maggiore, “Gravitational wave experiments and early universe cosmology,” [Phys. Rept.](#) **331** (2000) 283–367, [arXiv:gr-qc/9909001](#).
- [244] E. Thrane and J. D. Romano, “Sensitivity curves for searches for gravitational-wave backgrounds,” [Phys. Rev. D](#) **88** no. 12, (2013) 124032, [arXiv:1310.5300 \[astro-ph.IM\]](#).
- [245] C. Caprini, D. G. Figueroa, R. Flauger, G. Nardini, M. Peloso, M. Pieroni, A. Ricciardone, and G. Tasinato, “Reconstructing the spectral shape of a stochastic gravitational wave background with LISA,” [JCAP](#) **11** (2019) 017, [arXiv:1906.09244 \[astro-ph.CO\]](#).
- [246] T. Robens and T. Stefaniak, “Status of the Higgs Singlet Extension of the Standard Model after LHC Run 1,” [Eur. Phys. J. C](#) **75** (2015) 104, [arXiv:1501.02234 \[hep-ph\]](#).
- [247] A. Falkowski, C. Gross, and O. Lebedev, “A second Higgs from the Higgs portal,” [JHEP](#) **05** (2015) 057, [arXiv:1502.01361 \[hep-ph\]](#).
- [248] S. Dawson, P. P. Giardino, and S. Homiller, “Uncovering the High Scale Higgs Singlet Model,” [Phys. Rev. D](#) **103** no. 7, (2021) 075016, [arXiv:2102.02823 \[hep-ph\]](#).
- [249] D. Buttazzo, D. Redigolo, F. Sala, and A. Tesi, “Fusing Vectors into Scalars at High Energy Lepton Colliders,” [JHEP](#) **11** (2018) 144, [arXiv:1807.04743 \[hep-ph\]](#).
- [250] H. Al Ali et al., “The muon Smasher’s guide,” [Rept. Prog. Phys.](#) **85** no. 8, (2022) 084201, [arXiv:2103.14043 \[hep-ph\]](#).
- [251] P. S. B. Dev, R. N. Mohapatra, and Y. Zhang, “Leptogenesis constraints on $B - L$ breaking Higgs boson in TeV scale seesaw models,” [JHEP](#) **03** (2018) 122, [arXiv:1711.07634 \[hep-ph\]](#).
- [252] A. Ilnicka, T. Robens, and T. Stefaniak, “Constraining Extended Scalar Sectors at the LHC and beyond,” [Mod. Phys. Lett. A](#) **33** no. 10n11, (2018) 1830007, [arXiv:1803.03594 \[hep-ph\]](#).
- [253] F. F. Deppisch, W. Liu, and M. Mitra, “Long-lived Heavy Neutrinos from Higgs Decays,” [JHEP](#) **08** (2018) 181, [arXiv:1804.04075 \[hep-ph\]](#).
- [254] F. F. Deppisch, S. Kulkarni, and W. Liu, “Searching for a light Z' through Higgs production at the LHC,” [Phys. Rev. D](#) **100** no. 11, (2019) 115023, [arXiv:1908.11741 \[hep-ph\]](#).
- [255] S. Oda, N. Okada, and D.-s. Takahashi, “Right-handed neutrino dark matter in the classically conformal $U(1)'$ extended standard model,” [Phys. Rev. D](#) **96** no. 9, (2017) 095032, [arXiv:1704.05023 \[hep-ph\]](#).